NUMERICAL SIMULATION OF FLUID DYNAMICS AND TRANSPORT PHENOMENA IN ELECTROSTATICALLY CHARGED VOLATILE SPRAYS

Ajith Kumar Arumugham-Achari

Dipòsit Legal: T 1224-2014

Ajith Kumar Arumugham-Achari

Numerical simulation of fluid dynamics and transport phenomena in electrostatically charged volatile sprays

DOCTORAL THESIS

Department of Chemical Engineering

UNIVERSITAT ROVIRA I VIRGILI

Tarragona, 2014

Ajith Kumar Arumugham-Achari

Numerical simulation of fluid dynamics and transport phenomena in electrostatically charged volatile sprays

DOCTORAL THESIS

Supervised by

Dr. Jordi Grifoll i Taverna & Dr. Joan Rosell-Llompart

Department of Chemical Engineering

UNIVERSITAT ROVIRA I VIRGILI

Tarragona, 2014

Departament d'Enginyeria Quimica
Universitat Rovira i Virgili
Campus Sescelades,
Av. Països Catalans, 26
43007 Tarragona
Tel: 977559658
Fax: 977559667

Dr. Jordi Grifoll i Taverna and Dr. Joan Rosell-Llompart,

CERTIFY:

That the present study, entitled "Numerical simulation of fluid dynamics and transport phenomena in electrostatically charged volatile sprays" presented by Ajith Kumar Arumugham-Achari for the award of the degree of Doctor of Philosophy, has been carried out under our supervision at the Chemical Engineering Department of the University Rovira i Virgili, and that it fulfils the requirements to obtain the title.

Tarragona 12th June, 2014

Dr. Jordi Grifoll i Taverna Dr. Joan Rosell-Llompart

Acknowledgments

My heartfelt thanks to *Prof. Jordi Grifoll i Taverna* and *Prof. Joan Rosell Llompart* who jointly supervised this Ph.D. thesis. Prof. Jordi, through his vast knowledge in numerical methods, has been a constant source of knowledge, guidance and encouragement. Prof. Joan provided the most critical and intuitive inputs during our various discussions sharing his in-depth practical understanding on the fields of applied physics and electrosprays. Also, thanks to *Dr. Wilhelm* and *Dr. Pratsinis* for communicating on our request, the results of their simulations on electrospray evaporation.

This wouldn't have been possible without the earnest support of my family, especially my dearest wife *Vava* , son *Akash* and *Amma*, from whom I stole a considerable amount of time to pursue this endeavor. They were rock solid behind me whenever I needed them the most.

Special thanks to *Dr. Gitanjali Rai* for her support and kindness extended to me in this journey. She along with my other friends from India; *Shailesh, Pallavi, Sunil, Jagjit, Soumi, Venki* and *Sameer* are sure to bring me pleasant nostalgic memories of my stay in Tarragona.

I would like to thank *Ms. Eszter Bodnar*, *Nikolas* and *Dr. Luis Modesto* of the DEW (*Droplets, intErfaces and floWs*) research laboratory for their support and encouragement. I am also grateful to the able administrative assistance of secretaries (*DEQ*), *Ms. Nuria Juanpere* and *Ms. Merche* throughout this tenure.

Thanks to the financial support extended by the *Ministerio de Educación y Ciencia* (Government of Spain), via project CTQ2008-05758/PPQ & DPI2012-35687 and by the *Generalitat de Catalunya* (ref. 2009SGR-01529). Also acknowledged is the scholarship granted by *Universitat Rovira i Virgili* and the financial support of *DEW* research group.

And finally thanks to ***God*** who has always been kind to me!

To Vava, Kunjon and Amma

'Karmanye Vadhikaraste, Ma phaleshou kada chana,
Ma Karma Phala Hetur Bhurmatey Sangostva Akarmani'

(You have the right only to work, but never to its fruits. Let not the fruits of action be your motive. Nor let your attachment to results lead to inaction.)

-Bhagavad Gita

Table of contents

Summary

Electrosprays, which are generated as a result of the breakup of a liquid jet subjected to a sufficiently strong electric field, are constituted of highly charged micro drops moving under the action of electrostatic forces. The droplets hence generated are transported under the combined influence of the electrostatic gradient between the emitter needle and counterplate, the interaction with the spray charge and the aerodynamic drag force. Most of the applications of electrosprays involve droplet evaporation as a critical aspect in achieving their desired result . While many numerical models of electrosprays have neglected gas flow induced by the collective motion of the charged droplet cloud, experimental evidence shows that the gas speed can be significant locally in these systems. Also considering the importance it can have in droplet evaporation in volatile electrosprays, there is a need for a general methodology to include the induced gas flow caused by the droplets in current numerical models of electrospray dynamics. Furthermore, since the gas motion also influences the droplet motion, a formulation that can *accurately* describe these motions should be *fully coupled* (i.e., *two-way coupled*). Such improved models should be able to elucidate the influence of the induced gas flow on variables of practical importance such as the flux deposition pattern on the counterplate, plume spread, droplet number density distribution, and also in the prediction of droplet evaporation.

In view of these, we developed a numerical scheme which includes the gasflow induced by droplet motion in the numerical simulation of electrosprays. This thesis is organized in four chapters.

A general introduction on electrosprays, their applications, importance of numerical simulations for electrospray systems and the need of including the effects of induced gasflow in these simulations are described in Chapter 1.

An objective of this thesis in applying this computational scheme initially on a non-volatile electrospray system, is described in Chapter 2. Also explained in this chapter is the technique of employing Gaussian filters with variable kernel widths that depend on the droplet number density, in order to resolve the reactive drag force on the gas by the

droplets. We quantified the effect of induced gasflow on the characteristics of the droplet plume (viz., droplet number density, droplet velocity, droplet size distribution), as well as on droplet dynamics and mass flux, by applying this scheme to an experimentally characterized spray by Tang & Gomez (1994), which comprised of non-evaporating primary and satellite droplets in air. Results showed better agreement with the experimental data when airflow is taken into account than when it is not (assuming still air).

Electrospray applications usually involve volatile spray systems and gasflow being an important aspect in droplet evaporation, we further developed a comprehensive numerical scheme which fully couples the Lagrangian electrospray droplet dynamics with the effects of induced gasflow, Coulomb explosions, and the transport of solvent vapor as well as charge left over by vanishing droplets in such systems. The procedure to couple the different physics involved is discussed in Chapter 3.

Also discussed in this chapter is the application of this numerical scheme to compare the evaporation effects in three electrospray systems with solvents of different volatility, viz., acetone, methanol and n-heptane. Droplets were injected with unimodal and log-normal distributed diameters with a mean value of 8 μm, and a coefficient of variation of 10%. Steady state solutions for the electrospray system in Lagrangian framework and for the three Eulerian fields (gasflow dynamics, transport of vapor and charge left by vanishing droplets) were obtained, which helps to quantify the effects of various phenomena in a volatile electrospray system. The regions of intense Coulomb explosion events within the spray are well captured in form of diagonal bands (in the 2D domain). In all three cases, few or no droplets arrive at the counterplate located 3 cm down the capillary nozzle, highlighting the relevance of accounting for evaporation when simulating these systems. Conclusions from the present thesis work are elaborated in Chapter 4.

List of publications and conferences

Publications

1. Arumugham-Achari, A.K, Grifoll, J., & Rosell-Llompart, J. (2013). Two-way coupled numerical simulation of electrospray with induced gas flow. *J. Aerosol. Science, 65,* 121–133.
2. Arumugham-Achari, A.K, Grifoll, J., & Rosell-Llompart, J. (2014). Numerical simulations of evaporating electrosprays with Coulomb explosions. *J. Aerosol Science*: **(To be submitted)**

Conferences

1. Grifoll, J., Arumugham-Achari, A.K, & Rosell-Llompart, J. (2011). Numerical Simulation of Electrospray Droplets Dynamics, *V Reunión Española de Ciencia y Tecnología de Aerosoles (RECTA 2011); Madrid, Spain; 27-29 June 2011*: **Poster**
2. Arumugham-Achari, A.K, Grifoll, J., & Rosell-Llompart, J. (2013). Effects of induced gas flow on electrospray dynamics, *European Aerosol Conference (EAC 2013); Prague, Czech Republic; 01-06 September 2013*: **Oral presentation**
3. Arumugham-Achari, A.K, Grifoll, J., & Rosell-Llompart, J. (2014). Numerical simulations of evaporating electrosprays with Coulomb explosions, *Conference on Aerosol Technology 2014 (AT 2014); Karlsruhe, Germany; 16-18 June 2014*: **Oral presentation**

List of figures and schemes

Page

Chapter 1

Chapter 2

Chapter 3

List of tables

Page

Chapter 2

Chapter 3

Chapter 1

Chapter 1

Introduction

1.1 Electrosprays and their applications

Electrosprays are constituted of highly charged micro drops moving under the action of electrostatic forces. They are generated as a result of the breakup of a liquid jet subjected to a sufficiently strong electric field. In a simple electrospray system, to attain this, high voltage (~ in the order of several kV) is applied between the capillary needle (*emitter*) through which the liquid flows and the substrate plate (*counterplate*) on which the spray is deposited. *Fig. 1.1*a depicts the schematic sketch of the mechanism. The droplets hence generated are transported under the combined influence of the electrostatic gradient between the emitter and counterplate, the interaction with the spray charge and the aerodynamic drag force. Depending upon the liquid flow rate, and voltage applied between the electrodes, electrosprays can exhibit different modes, viz. dripping, pulsation, cone-jet, and multi-jet. *Fig. 1.1b* shows the photograph of an electrospray in cone-jet mode.

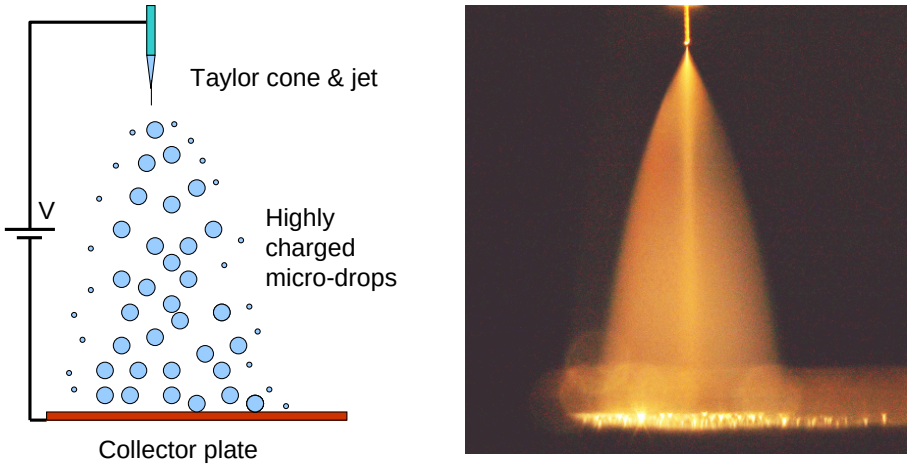

Fig. 1.1 (a) Schematic diagram of a simple electrospray mechanism. (b) an electrospray in cone-jet mode

Since it is possible to extensively control the fineness of such particles by varying the applied voltage, liquid flow rate, electrode configuration, and the mechanical and electrical properties of the liquid (Cloupeau & Prunet-Foch, 1994), they promise extensive applications in the field of drug delivery, agricultural and automotive sprays, ink-jet printers, particle synthesis (Barrero & Loscertales, 2007; Jaworek & Sobczyk, 2008; Bock et al 2012), production of thin and uniform coatings (Leeuwenburgh et al., 2006; Jaworek, 2007; de Jonge et al., 2009; Roncallo et al., 2010; Martin et al., 2010), space thrusters (Gamero-Castaño, 2008; Krpoun & Shea, 2009), and mass spectrometry (ESI-MS) (Fenn et al., 1989; Fenn, 2003) etc.

1.2 Induced gasflow and electrospray droplet evaporation

When a collection of aerosol particles move with a net velocity relative to the surrounding gas, it exerts a drag force on the gas which can cause the gas to flow. In electrosprays, this gas motion is induced by the highly charged micro-drops moving under the action of electrostatic forces. *Fig 1.2* illustrates the mechanism of induced gas motion, and the reactive drag force on air as contributed by an individual droplet. In this figure, $\mathbf{F_i}$ is the reactive drag force on gas due a droplet of size d_i moving with the velocity $\mathbf{V_i}$. ρ_f is the density of gas and $\mathbf{u}$ is the mean gas velocity.

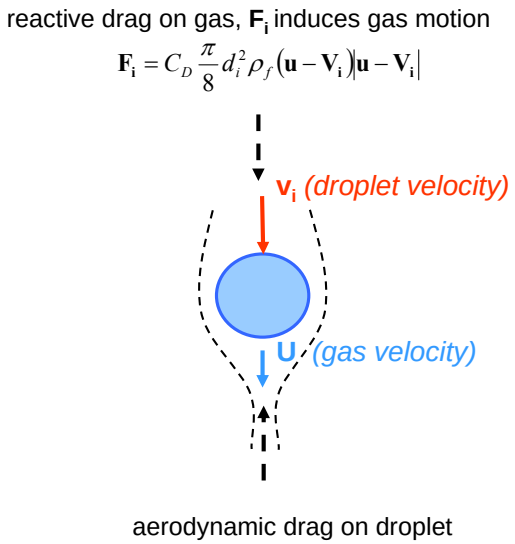

Fig 1.2. Schematic sketch of induced gas motion due to droplet drag

Because of the difficulty in experimentally assessing gas velocity in electrosprays, only a handful of reports have addressed the question of gas flow induced by the droplet motion. Tang & Gomez (1994), while carrying out a detailed experimental study on the structure of a heptane electrospray, measured gas velocities along the spray centerline as high as 34% of the droplet axial velocity. Hartman et al. (1999) found that while droplet diameters do not vary radially, their axial velocity dropped as much as 40% from its centerline value. They took this result to mean that the gas must move with a significant axial velocity at the electrospray centerline.

Droplet evaporation is a critical aspect aimed at producing the desired result in many applications of the electrosprays, mentioned in *Section 1.1*. For example, the extent of droplet evaporation determines the variety of product morphologies that can be achieved via electrospray deposition (Rietveld et al, 2006, Bodnár & Rosell-Llompart, 2013). Also as the charged droplets evaporate, their charge to mass ratio increases, and undergoes droplet fission (Coulomb explosions) on reaching the Rayleigh limit which is given by

$$q = q_R = \sqrt{\left(8\pi^2 \varepsilon_o \gamma d^3\right)} \qquad (1)$$

where q is the charge held by a droplet of diameter d, q_R is the charge at Rayleigh limit, ε_0 is the permittivity of vacuum and γ is the surface tension of liquid in air. By these explosions a parent droplet releases mass and charge through a number of progenies. *Fig. 1.3* is the schematic sketch of an evaporating electrospray droplet.

In sum, since gas motion can be a significant factor in droplet evaporation, its study has relevance in the field of volatile electrospray systems.

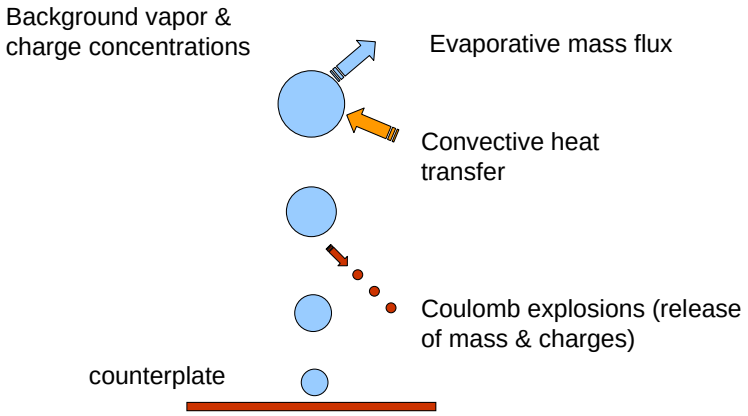

Fig. 1.3. Schematic sketch of an evaporating electrospray droplet

1.3 Numerical simulations on electrospray systems

The first reported numerical simulation of droplet dynamics in a non-volatile electrospray is by Gañan-Calvo et al. (1994), who assumed that the surrounding gas is still. The constituent terms of their Lagrangian model are the electrical forces produced by the external field (due to the electrodes) and by the space charge (droplet–droplet Coulombic repulsion, including image charges at the counterplate), and the drag force on the droplets due to friction with the gas. This general model has subsequently been followed to simulate various non-volatile electrospray systems by different authors, viz., Hartman et al. (1999), Wilhelm et al. (2003), Oh et al. (2008), Jung et al. (2010), Yang et al. (2012) and Grifoll & Rosell-Llompart (2012, 2014). The still gas assumption has also been followed in the recent Eulerian model of Higuera (2012). The assumption of the gas to be still has been followed in most of the numerical simulations as a matter of convenience, given the complexity of the endeavor.

The numerical works that have simulated volatile electrosprays are the studies by Wilhelm et. al (2003) and Sen et. al (2011). In both of these, the spray system was assumed to evaporate against zero solvent background vapor concentration in still ambient conditions, wherein the droplet fission was considered. No account for including the airflow was done, and under this assumption diffusion alone contributed to vapor transport. Furthermore, any corrections in the electrostatic field due to charges left behind by the fully evaporating droplets were not described in these works.

However, in some of these works, the assumption of still gas has been justified based on conservation arguments about the global influence of the droplet motion on the gas. Gañan-Calvo et al. (1994) obtained the characteristic droplet velocity by balancing viscous drag to electric force. By globally balancing the energy transferred per unit time to the gas by the spray drag, with the energy dissipated by the viscous stresses outside the spray boundaries, they estimate that the characteristic (average) gas velocity is much smaller than the characteristic droplet velocity. Wilhelm et al. (2003), while evaluating the extent of droplet evaporation, applied global momentum balance to their electrospray system estimate the average gas velocity to be 0.4 m/s, which falls between 3.7% of their highest axial droplet velocity and 11.7% of their lowest one. Higuera (2012) justified

neglecting the gas motion in his Eulerian simulation after an order of magnitude estimation of the momentum exchanged between the droplets and the gas.

Since the conservation arguments are based on radially averaged variables, they can overlook regions of high local gas velocity. Therefore, they are not in contradiction with the experimental determinations of high centerline gas velocities which were mentioned earlier. Indeed, using a more detailed approach, Hartman et al. (1999) estimated that the gas velocity close to the spray centerline could be around 32% of droplet axial velocities. They arrived at this conclusion by balancing the electric power of the system with the kinetic power of the induced gas flow (confined within a radius) and the kinetic power of the droplets.

Deng & Gomez (2007) are the first to partially include the effect of gas flow on the droplet drag calculations, by treating the early stage of the spray as a continuous cylindrical surface, and adopting a boundary layer sub-model based on the momentum integral of a logarithmic gas velocity profile.

1.4 Objectives of this thesis

While many numerical models have neglected induced gas flow, the experimental evidence shows that the gas speed can be significant locally. Also considering the importance it can have in droplet evaporation in volatile electrosprays, there is a need for a general methodology to include the induced gas flow caused by the droplets in current numerical models of electrospray dynamics. Furthermore, since the gas motion also influences the droplet motion, a formulation that can *accurately* describe these motions should be *fully coupled* (i.e., *two-way coupled*). Such improved models should be able to elucidate the influence of the induced gas flow on variables of practical importance such as the flux deposition pattern on the counterplate, plume spread, droplet number density distribution, and also in the prediction of droplet evaporation. In view of these, the objectives of this thesis can be summarized as follows:

- To develop a numerical scheme which includes the gasflow induced by droplet motion in the numerical simulation of electrosprays.

- To quantify the effect of induced gasflow on the characteristics of the droplet plume (droplet number density, droplet velocity, droplet size distribution), as well as on droplet dynamics and mass flux. To verify the results against the experimental values in a non-volatile electrospray system, and also to compare such results with the simulations assuming still air.

- To develop a comprehensive numerical scheme which fully couples electrospray droplet dynamics with the effects of induced gasflow, Coulomb explosions, and the transport of solvent vapor as well as charge left over by vanishing droplets in volatile electrospray systems. To develop separate codes for the same.

- To apply the fully coupled numerical scheme in predicting the behavior of three electrospray systems of varying volatility.

1.5 References

Barrero, A., & Loscertales, I. G., (2007). Micro- and Nanoparticles via Capillary Flows, *Annual Review of Fluid Mechanics*, 39, 89-106

Bock, N., Dargaville, T.R., Woodruff, M.A. (2012). Electrospraying of polymers with therapeutic molecules: State of the art, *Progress in Polymer Science*, *37*, 1510-1551.

Bodnár, E. & Rosell-Llompart, J. (2013). Growth dynamics of granular films produced by electrospray, *J. Coll. Int. Sci.*, submitted.

Cloupeau, M., & Prunet-Foch, B (1994 Electrohydrodynamic Spraying Functioning modes: a critical review, *Journal of Aerosol Science: Special issue on "Electrospray Science and Applications", **25(**6),* 1021-1036.

Deng, W., & Gomez, A. (2007). Influence of space charge on the scale-up of multiplexed electrosprays. *J. Aeros. Sci., 38,* 1062-1078.

Fenn, J.B., Mann, M., Meng, C.K., Wong, S.F., & Whitehouse, C.M. (1989). Electrospray ionization for mass spectrometry of large biomolecules, *Science, 246* (4926), 64-71.

Fenn, J. B. (2003). Electrospray wings for molecular elephants (Nobel lecture), *Angew. Chem.-Int. Ed., 42*(33): 3871-3894.

Gamero-Castano, M. (2008). The structure of electrospray beams in vacuum. *J. Fluid Mech.*, *604*, 339-368.

Gañan-Calvo, A. M., Lasheras, J.C., Davila, J., & Barrero, A. (1994). The electrostatic spray emitted from an electrified conical meniscus. *J. Aeros. Sci., 25*, 1121-1142.

Grifoll, J. & Rosell-Llompart, J. (2012). Efficient Lagrangian simulation of electrospray droplets dynamics. *J. Aeros. Sci., 47*, 78-93.

Grifoll, J. & Rosell-Llompart, J. (2014). Continuous droplets' charge model for the Lagrangian simulation of 2 electrostatic sprays, *submitted to J. Electrostatics*

Hartman, R. P. A., Borra, J. P. , Brunner, D. J. , Marijnissen, J. C. M., & Scarlett, B. (1999). The evolution of electrohydrodynamic sprays produced in the cone-jet mode, a physical model. *J. Electrostat.*, *47*, 143-170.

Higuera, F. J. (2012). Eulerian model of a dilute spray of charged droplets. *J. Aeros. Sci., 48,* 34-45.

Jaworek, A. (2007). Electrospray droplet sources for thin film deposition. *J. Mater. Sci., 42,* 266-297.

Jaworek, A. & Sobczyk, A.T. (2008). Electrospraying route to nanotechnology: An overview. *J. Electrostat., 66*, 197-219.

Jung, J. H., Oh, H., & Kim, S. S. (2010). Numerical simulation of the deposition pattern in multiple electrohydrodynamic spraying. *Powder Technol.*, *198*, 439-444.

Krpoun, R., & Shea, H. R., (2009). Integrated out-of-plane nanoelectrospray thruster arrays for spacecraft propulsion. *J. Micromech Microeng.*, *19(4)*, 045019

Oh, H., Kim, K., & Kim, S. (2008). Characterization of deposition patterns produced by twin-nozzle electrospray. *J. Aeros. Sci.*, *39*, 801-813.

Rietveld, I. B., Kobayashi, K., Yamada H., & Matsushige, K. (2006). Electrospray deposition, model, and experiment: Toward general control of film morphology. *J. Phys. Chem. B*, *110*, 23351-23364.

Roncallo, S., J. D. Painter, S. A. Ritchie, M. A. Cousins, M. V. Finnis, K. D. Rogers, (2010). Evaluation of different deposition conditions on thin films deposited by electrostatic spray deposition using a uniformity test, *Thin Solid Films, 518* (17), 4821-4827.

Rosell-Llompart, J. & Fernandez de la Mora., J. (1994). Generation of monodisperse droplets 0.3 to 4 μm in diameter from electrified cone-jets of highly conducting and viscous liquids. *J. Aeros. Sci., 25*, 1093-1119.

Sen, A.K., Darabi, J., & Knapp, D. R. (2011) Aerosol Formation in Electrospray Ionization Using a Microfluidic Emitter. *IEEE Sensors Journal, 11*(10), 2335-2341

Tang, K. & Gomez, A. (1994). On the structure of an electrostatic spray of monodisperse droplets. *Phys. Fluids, 6*, 2317-2332.

Wilhelm, O., Madler, L., & Pratsinis, S. E. (2003). Electrospray evaporation and deposition. *J. Aeros. Sci.*, *34*, 815-836.

Yang, W., Lojewski, B., Wei, Y., & Deng, W. (2012). Interactions and deposition patterns of multiplexed electrosprays. *J. Aerosol Sci., 46,* 20-33.

Chapter 2

Chapter 2

Two-way coupled numerical simulation of electrospray with induced gas flow[a]

2.1 Abstract

The gas flow induced by droplet motion has been included in the numerical simulation of electrosprays. Steady state solutions were sought iteratively in a computational scheme that fully couples a 3D Lagrangian model for the droplet dynamics with a steady state 2D axisymmetric Eulerian model for the induced gas flow. To resolve the reactive drag force on the gas by the droplets we employ Gaussian filters with variable kernel widths that depend on the droplet number density. We have applied this scheme to an experimentally characterized spray from the literature comprised of non-evaporating primary and satellite droplets in air. The predicted characteristics of the droplet plume (droplet number density, droplet velocity, droplet size distribution) better match the experimental values when the induced airflow is accounted for than when it is not (assuming still air). It is shown that the induced airflow contributes to faster moving droplets, shrinkage of plume, and a prominent flux about the spray axis (centerline), as compared with the simulations assuming still air. Induced airflow results in an increase of 80% in axial droplets velocity at the centerline at the collection counterplate. The ratio of mass flux at the centerline between the cases of moving and still air equals 2.6 at the counterplate. We have also observed that the radial segregation by size of the satellite droplets is sensitive to the functional relationship between their charge-to-mass ratio and diameter. Induced gas flow is expected to have important implications in the simulation of droplet evaporation and vapor concentration in electrosprays.

Keywords: Electrospray, Lagrangian simulation, Induced gas flow, Numerical simulation, Spray dynamics, Deposition.

[a] ***Results published in J. Aer. Sci: http://dx.doi.org/10.1016/j.jaerosci.2013.07.005***

Nomenclature

Roman letter symbols

a	factor in the relationship between ξ and d_i (Cm^{-b}/kg,)
b	exponent in the relationship between ξ and d_i
$\mathbf{d}$	ensemble averaged reactive drag force density (N/m^3)
$\mathbf{d'}$	fluctuating component of reactive drag force density (N/m^3)
D_c	capillary tube outer diameter (m)
$\mathbf{D}$	instantaneous reactive drag force density (N/m^3)
C_D	droplet drag coefficient
d_i	diameter of i-th droplet (m)
d_{jet}	electrospray jet diameter (m)
$\overline{d}_p$	count mean primary droplet diameter (m)
$\overline{d}_s$	count mean satellite droplet diameter (m)
$\mathbf{E_{ext}}$	external electrical field (V/m)
$\mathbf{F_i}$	drag force acting on droplet i (N)
$\mathbf{F_i^k}$	drag force acting on droplet i at stage k (N)
$\mathbf{F_{elec,i}}$	electric force acting on droplet i (N)
H	capillary tube tip to counterplate distance (m)
K	Kernel function
K_{Gauss}	Gaussian kernel function
N	number of droplets
n	local ensemble-averaged droplet number density
N_R	number of system realizations for ensemble averaging
p	average pressure (Pa)

p' fluctuating pressure (Pa)

P instantaneous pressure (Pa)

q_i electrical charge of droplet i (C)

Q liquid flow rate (m^3/s)

r polar coordinate (m)

Re_i $\left(= \frac{\rho_f |\mathbf{u} - \mathbf{V_i}| d_i}{\mu}\right)$ Reynolds number

$\mathbf{R_i}$ ($= [x_i, y_i, z_i]$) position vector of i-th droplet (m)

$\mathbf{R_i^k}$ position vector of i-th droplet at stage k (m)

$\mathbf{R_I}$ ($= [x_i, y_i, 2H - z_i]$) position vector of image of i-th droplet on counterplate (m)

$\mathbf{R_{ij}}$ ($= \mathbf{R_i} - \mathbf{R_j}$) displacement between the position vectors of droplets i and j (m)

$\mathbf{R_{iJ}}$ ($= \mathbf{R_i} - \mathbf{R_J}$) displacement between the position vectors from the image of droplet j on the counterplate to droplet i (m)

s average separation between the centers of neighboring droplets in the ensemble spray (m)

SD_p Standard deviation of primary droplets' diameters distribution (m)

SD_s Standard deviation of satellite droplets' diameters distribution (m)

$\boldsymbol{t}$ time (s)

$\mathbf{u}$ mean gas velocity vector (m/s)

$\mathbf{u'}$ fluctuating component of gas velocity vector (m/s)

$\mathbf{U}$ instantaneous gas velocity vector (m/s)

V volume of the spray (m^3)

$\mathbf{V_i}$ velocity vector for droplet i (m/s)

V_{jet} electrospray jet velocity (m/s)

$\mathbf{x}$ ($=[x,y,z]$) position vector (m)

z_e	droplet emission point (m)

Greek letter symbols

α	normalization factor
δ	Dirac's delta function
ε_0	electrical permittivity of vacuum (8.854×10^{-12} C/V·m)
ξ	droplet charge to mass ratio (C/kg)
$\overline{\xi}_p$	average charge to mass ratio of primary droplets (C/kg)
$\overline{\xi}_s$	average charge to mass ratio of satellite droplets (C/kg)
$\boldsymbol{\lambda}$	(= $\mathbf{x} - \mathbf{R_i}$) displacement between the position vector $\mathbf{x}$ and position of droplet i (m)
μ	dynamic viscosity of surrounding gas (kg/m·s)
ϕ	electrostatic potential (V)
Φ_0	electrostatic potential at the capillary tube (V)
ρ_d	density of drop liquid (kg/m^3)
ρ_f	density of surrounding gas (kg/m^3)
σ	Gaussian kernel width (m)

Acronyms

CFD	Computational Fluid Dynamics
RANS	Reynolds-averaged Navier-Stokes
CVFD	Control Volume Finite Difference
LSC	Lumped Space Charge
OD	Outer diameter

2.2. Introduction

Electrosprays are dense clouds of highly charged micro drops that are set in motion by the action of external electrostatic fields. Such collections of aerosol particles move with a

net velocity relative to the surrounding gas and, as a result, exert a reactive drag force on the gas, which induces gas flow. This gas motion can be significant in the study of electrospray dynamics, particularly when droplet evaporation is involved. Droplet evaporation is a key process for many applications of electrospray, such as electrospray ionization mass spectrometry (ESI-MS) (Fenn et al, 1989; Fenn, 2003), particle synthesis by electrospray (Jaworek & Sobczyk, 2008; Bock et al 2012), and electrospray deposition for the synthesis of thin films and coatings (Jaworek, 2007), in which the extent of droplet evaporation determines whether a film will be granular (Bodnár & Rosell-Llompart, 2013) or display a range of film morphologies (Rietveld et al, 2006).

Because of the difficulty in the experimental accessibility to gas velocity in electrospray systems, only a few experimental reports have addressed the question of gas flow induction by the droplet motion. Tang & Gomez (1994), while carrying out a detailed experimental study on the structure of a heptane electrospray, measured gas velocities along the spray centerline as high as 34% of the droplet axial velocity. Hartman et al. (1999) found that while droplet diameters do not vary radially, their axial velocity dropped as much as 40% from its centerline value. They took this result to mean that the gas must move with a significant axial velocity at the electrospray centerline.

Our ability to predict the induced gas flow pattern is currently very limited because we lack general methodologies for predicting it. The majority of numerical simulation works have assumed the gas to be still as a matter of convenience, given the complexity of the endeavor. The first reported numerical simulation of droplet dynamics in an electrospray is by Gañan-Calvo et al. (1994), who assumed that the surrounding gas is still. The constituent terms of their Lagrangian model are the electrical forces produced by the external field (due to the electrodes) and by the space charge (droplet–droplet Coulombic repulsion, including image charges at the counterplate), and the drag force on the droplets due to friction with the gas. This general model has subsequently been followed to simulate various electrospray systems by different authors, viz., Hartman et al. (1999), Wilhelm et al. (2003), Oh et al. (2008), Jung et al. (2010), Yang et al. (2012) and Grifoll & Rosell-Llompart (2012). The still gas assumption has also been followed in the recent Eulerian model of Higuera (2012).

In some of these works, the assumption of still gas has been justified based on conservation arguments about the global influence of the droplet motion on the gas.

Gañan-Calvo et al. (1994) obtained the characteristic droplet velocity by balancing viscous drag to electric force. By globally balancing the energy transferred per unit time to the gas by the spray drag, with the energy dissipated by the viscous stresses outside the spray boundaries, they estimate that the characteristic (average) gas velocity is much smaller than the characteristic droplet velocity. Wilhelm et al. (2003), while evaluating the extent of droplet evaporation, applied global momentum balance to their electrospray system estimate the average gas velocity to be 0.4 m/s, which falls between 3.7% of their highest axial droplet velocity and 11.7% of their lowest one. Higuera (2012) justified neglecting the gas motion in his Eulerian simulation after an order of magnitude estimation of the momentum exchanged between the droplets and the gas.

Since the conservation arguments are based on radially averaged variables, they can overlook regions of high local gas velocity. Therefore, they are not in contradiction with the experimental determinations of high centerline gas velocities which were mentioned earlier. Indeed, using a more detailed approach, Hartman et al. (1999) estimated that the gas velocity close to the spray centerline could be around 32% of droplet axial velocities. They arrived at this conclusion by balancing the electric power of the system with the kinetic power of the induced gas flow (confined within a radius) and the kinetic power of the droplets.

Deng & Gomez (2007) are the first to partially include the effect of gas flow on the droplet drag calculations, by treating the early stage of the spray as a continuous cylindrical surface, and adopting a boundary layer sub-model based on the momentum integral of a logarithmic gas velocity profile.

In sum, while many numerical models have neglected induced gas flow, the experimental evidence shows that the gas speed can be significant locally (at the centerline). Therefore, there is a need for a general methodology to include the induced gas flow caused by the droplets in current numerical models of electrospray dynamics. Furthermore, since the gas motion also influences the droplet motion, a formulation that can *accurately* describe these motions should be *fully coupled* (i.e., *two-way coupled*). Such improved models should be able to elucidate the influence of the induced gas flow on variables of practical importance such as the flux deposition pattern on the counterplate, plume spread, droplet number density distribution, and also in the prediction of droplet evaporation.

In the present work, we have developed a two-way coupled Lagrangian description of the droplet dynamics with an Eulerian description of the induced gas flow. The gas flow description does not consider the detailed flow around each droplet. Instead, two-way coupling is attained by seeking time-averaged pseudo-steady state solutions in both frameworks (droplet dynamics and induced gas flow). The predictive capability of this methodology is assessed by applying it to the experimentally characterized system of Tang & Gomez (1994) which considers non-evaporating droplets.

2.3. Methodology

We propose a numerical method that solves for the droplet dynamics and the gas flow using an iterative procedure, and seeks pseudo-steady state solutions using separate codes for the droplet and gas transport equations. The motion of non-coalescent, non-evaporating droplets under electric forces in moving gas is simulated by a 3D Lagrangian particle tracking model. The droplet-induced pseudo-steady gas flow is simulated by a 2D axisymmetric Eulerian model. All of the space within the spray is available to the gas, since the volume fraction of the droplet phase is much smaller than unity (dilute aerosol approximation).

2.3.1. Governing equations

2.3.1.1 Lagrangian 'particle dynamics'

The 3D Lagrangian droplet dynamics simulations are based on the model first proposed by Gañán-Calvo et al (1994). The electrospray system is considered to be made of electrostatically interacting droplets considered to be point particles for which the mutual aerodynamic interactions are not considered. The droplets also experience drag from the surrounding gas, and interact with an external electrostatic field created by electrodes (a droplet-emitting capillary tube, and a droplet-collecting plate named *counterplate*). Following these assumptions, the droplet dynamics are described by Newton's second law:

$$\frac{\pi}{6} d_i^3 \rho_d \frac{d\,\mathbf{V_i}}{d\,t} = \mathbf{F_i} + \mathbf{F_{elec,\,i}} \qquad (1)$$

where $\mathbf{F_i}$ and $\mathbf{F_{elec,i}}$ are the drag and electric forces acting on droplet *i*, which are given by:

$$\mathbf{F_i} = C_{Di}\frac{\pi}{8}d_i^2\rho_f\left(\mathbf{u}-\mathbf{V_i}\right)\left|\mathbf{u}-\mathbf{V_i}\right| \tag{2}$$

where

$$C_{Di} = \frac{24}{Re_i}\left(1+0.1104\sqrt{Re_i}\right)^2 \tag{3}$$

which is valid for $Re_i < 5000$ (Abraham 1970), and

$$\mathbf{F_{elec,\,i}} = q_i\mathbf{E_{ext}} + \frac{q_i}{4\pi\varepsilon_0}\sum_{\substack{j=1\\ j\neq i}}^{N} q_j\left(\frac{\mathbf{R_{ij}}}{R_{ij}^3}-\frac{\mathbf{R_{iJ}}}{R_{iJ}^3}\right) \tag{4}$$

The motion of a droplet *i* is described by its position vector $\mathbf{R_i}$ and velocity vector $\mathbf{V_i}$, as

$$\frac{d\,\mathbf{R_i}}{d\,t} = \mathbf{V_i} \tag{5}$$

Equations (1) and (5) are solved for each droplet to obtain its trajectory from the emission point to the counterplate.

2.3.1.2. Gasflow dynamics and boundary conditions

The body force impelling the gas flow is the reactive drag force due to the droplets' motions. Therefore, the gas motion is governed by the continuity equation (assuming incompressible gas flow) and the Navier-Stokes (momentum transport) equations extended to include droplet drag forces:

$$\nabla\cdot\mathbf{U} = 0 \tag{6}$$

$$\rho_f\left(\frac{\partial\mathbf{U}}{\partial t}+\mathbf{U}\cdot\nabla\mathbf{U}\right) = -\nabla P+\mu\nabla^2\mathbf{U}+\mathbf{D} \tag{7}$$

where **D** is a fine grained function that describes the reactive drag force per unit volume exerted by the droplets on the gas, which, when droplets are modeled as material points, is given by

$$\mathbf{D}(\mathbf{x}) = \sum_{i=1}^{N} (-\mathbf{F_i})\, \delta(\mathbf{x} - \mathbf{R_i}) \tag{8}$$

The instantaneous flow velocity, pressure and reactive drag force density are split into their time-averaged and fluctuating components as

$$\mathbf{U} = \mathbf{u} + \mathbf{u}' \tag{9}$$

$$P = p + p' \tag{10}$$

$$\mathbf{D} = \mathbf{d} + \mathbf{d}' \tag{11}$$

In the present work, we seek to determine the time-averaged gas flow field $\mathbf{u}$. Hence, Eq. (7) is time-averaged in order to obtain the steady-state fluid flow equation, which is similar to RANS equation in turbulent flows, i.e.

$$\rho_f\, \mathbf{u} \cdot \nabla \mathbf{u} = -\nabla p + \mu \nabla^2 \mathbf{u} - \rho_f \nabla \cdot \left(\overline{\mathbf{u}'\mathbf{u}'}\right) + \mathbf{d} \tag{12}$$

where $\rho_f \overline{\mathbf{u}'\mathbf{u}'}$ is analogous to the Reynolds stress term in turbulent flow, though different in its cause. In order to account for this viscous-like stress in Eq. (12), a closure model would be needed. This closure model could be formulated either by comparing system-specific solutions of Eqs. (6-7), or detailed experimental data, to Eq. (12). Here, the gas velocity perturbations $\mathbf{u}'$ are associated with the local perturbations on the gas mean flow caused by passing droplets. Therefore, such system-specific solutions or data would have to resolve very fine flow scales, and thus present enormous difficulties. Any such approach is beyond the scope of the present formulation, in which, as a first approximation, the term $\rho_f \nabla \cdot \left(\overline{\mathbf{u}'\mathbf{u}'}\right)$ is neglected.

The computational domain and boundary conditions for the gas flow are 2D axisymmetric, as shown in *Fig.2.1*. The surfaces of the cylindrical capillary tube electrode and the counterplate are assumed to be stationary walls with no-slip conditions imposed on them. The gas is free to flow in and out through the open boundaries, in such a way that the flow is normal at the top boundary and fulfills a self similarity condition at the side boundary (Deshpande & Vaishnav, 1982). The jet extends from below the capillary tube (Fig. 1), and moves with velocity V_{jet} which is estimated from the total flow rate and

d_{jet} by the mass conservation principle ($=4Q/\left(\pi d_{jet}^2\right)$). The surface of the electrospray jet is modeled as a cylindrical boundary of uniform diameter d_{jet}, which can be estimated from the count mean droplet diameter as $\bar{d}_p/1.89$ (Tang & Gomez, 1994; Rosell-Llompart & Fernandez de la Mora, 1994).

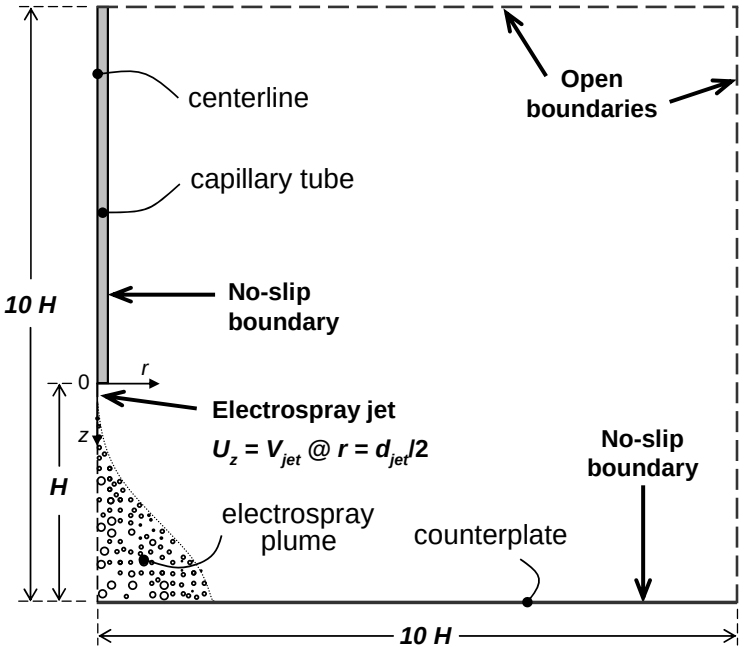

Fig. 2.1. Schematic diagram of the 2D axisymmetric computational domain for the gas flow, including boundary conditions.

2.3.1.3. Ensemble averaged reactive drag force

In Eq. (12) the reactive drag force density **d** can be computed by ensemble averaging Eq. (8) over a large number N_R of system realizations (ergodic hypothesis). N_R is defined as "large" enough to make **d** become independent of N_R. In addition, the fine grained (singular) description based on Dirac's delta must be replaced with a coarser grained (non-singular) kernel function K such that

$$\mathbf{d}(\mathbf{x}) = \frac{1}{N_R}\sum_{k=1}^{N_R}\sum_{i=1}^{N}\left(-\mathbf{F}_\mathbf{i}^\mathbf{k}\right)K\left(\mathbf{x}-\mathbf{R}_\mathbf{i}^\mathbf{k}\right) \tag{13}$$

In this work we employ the *Gaussian kernel* defined as

$$K_{Gauss}(\boldsymbol{\lambda}) = \alpha \frac{\exp\left[-|\boldsymbol{\lambda}|^2/(2\sigma^2)\right]}{\sigma^3} \tag{14}$$

where σ is the filter width for smoothing the reactive drag forces, and α is a normalization factor that ensures conservation of force globally within the ensemble averaged system, so that

$$\sum_{k=1}^{N_R}\sum_{i=1}^{N}\left(-\mathbf{F}_\mathbf{i}^\mathbf{k}\right) = N_R \int_{\substack{\text{spray}\\\text{volume}}} \mathbf{d}(\mathbf{x})\, dV \quad . \tag{15}$$

Similar smoothing of the particle drag force has been employed in numerical simulations of particle laden flows (Kitagawa et al, 2001; Maxey & Patel, 2001; Apte et al, 2008; Finn et al, 2011).

Deen et al. (2004) suggest that the filter width should be in the order of particle diameter, rather than at finer length scales. This is a logical consequence of the fact that each droplet transfers its drag to the gas phase at the droplet surface. Kim et al. (1993) simulated three-dimensional flow over two fixed spheres normal to the line connecting their centers, for $50 < Re < 150$. They found that the drag increases as the spheres become close together, and that the drag coefficient for separations larger than four diameters differs by less than 0.7% of the drag for an isolated single sphere. Since the kernel width should not be smaller than the "region of influence" of the drag force, the smallest kernel width extends to about two droplet diameters in this study.

At the same time, our formulation is tolerant of filter widths that are larger than the particle diameter, as long as $\mathbf{d}(x, y, z)$ remains unchanged. This can happen when σ is sufficiently smaller than the characteristic distance for maximum change of $\mathbf{d}$:

$$\sigma << \frac{|\mathbf{d}|}{|\nabla \mathbf{d}|_{\max}} \tag{16}$$

Finally note that any choice of filter width σ implies a large enough ensemble (large enough N_R), such that the density force field becomes independent of the ensemble size. In other words, the graininess of the ensemble spray should not be "imprinted" onto $\mathbf{d}(x, y, z)$, which, instead, should be a smooth function of position. In mathematical terms, in the ensemble spray the droplet centers must be much closer together than the filter width σ:

$$\sigma >> s \equiv \left(nN_R\right)^{-1/3},$$

where n is the local ensemble-averaged droplet number density, and s is the average separation between the centers of neighboring droplets in the ensemble spray. Therefore N_R must fulfill:

$$N_R >> \frac{1}{n\sigma^3} \tag{17}$$

2.3.2. Numerical implementation

The numerical scheme has been implemented in three parts: droplet dynamics, reactive drag force calculation, and gas flow dynamics. These parts have been run iteratively through successive stages according to the flow chart shown in *Fig.2. 2*. Initially (stage 0), quiescent gas is assumed (**u** = 0) and the droplet dynamics is simulated long enough to ensure that a statistically significant portion of the steady state is captured (Grifoll & Rosell-Llompart, 2012). Using this solution, an ensemble-averaged drag force field is computed. Such field is then used with the gas dynamics code to compute the steady-state velocity field solution. This solution is then fed back into the droplet dynamics simulation, initiating a new stage of the global iteration loop. The overall scheme is considered to have converged by comparing the gas flow solutions of two consecutive stages. A more detailed description of these steps is provided next.

2.3.2.1. Droplet dynamics and the reactive drag force calculation

The present 3D Lagrangian droplet dynamics simulations use the LSC method of Grifoll & Rosell-Llompart (2012). This scheme simplifies the far droplet-droplet electrostatic interactions (last term of Eq. (4)) using a coarse-graining approximation without any significant loss in accuracy.

Upon attaining a droplet dynamics solution, the droplets' relative velocities $\mathbf{(V_i - u)}$ and position data $\mathbf{R_i}$ are used to compute the corresponding drag forces $\mathbf{F_i}$ (Eq. (2)). Next, through the methodology explained in *Section 2.3.1*, the fine grained reactive drag force data are ensemble averaged over N_R realizations. Then, they are smoothed in a 3D Cartesian grid of cubic elements of side equal to the kernel width. And these smoothed

data are then transformed from the 3D Cartesian domain to the 2D cylindrical domain in which the computation of gas flow is carried out (*Fig.2.1*).

2.3.2.2. Gas flow dynamics

The 2D Eulerian gas flow computations are based on the stream function-vorticity formulation and on the Control Volume Finite Difference (CVFD) discretization scheme proposed by Gosman et al. (1969). The CVFD methodology is an integral approach which considers control volumes, each surrounding a computational node. It has the advantages of ensuring the conservation laws and ease of physical interpretation and implementation. More details of this discretization scheme and the solution procedure can be found in Deshpande & Vaishnav (1982). The numerical scheme was tested against the laminar jet problem of Deshpande & Vaishnav (1982), resulting in better than 2% agreement in the stream function values.

At each iteration stage (*Fig. 2.2*), the computed gas flow field is fed to the droplets dynamics code in order to update the spray configuration. The drag forces on the droplets are re-calculated according to Eq. (2) where the updated gas velocity at the droplets positions is interpolated from its values at the neighboring grid points. Since the variation in velocities between contiguous grid points is small, we opt for zero-order interpolation, namely taking the gas velocity value of the cell to which each droplet belongs.

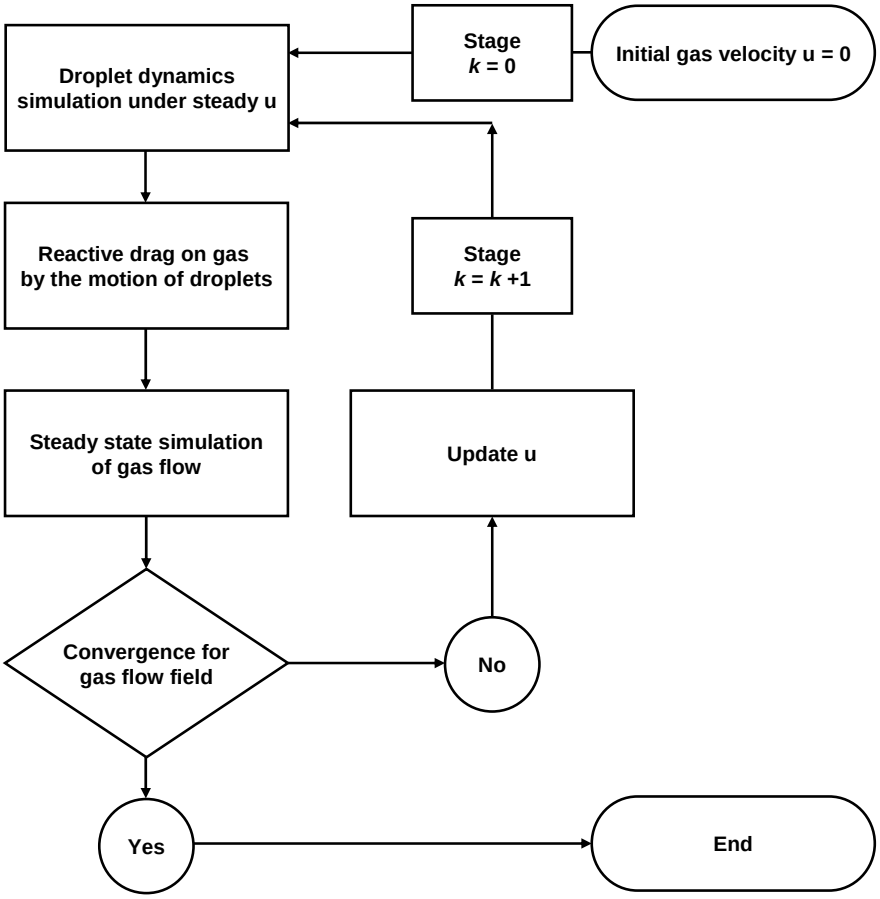

Fig. 2.2. Numerical scheme for two-way coupling.

2.4. Results and discussion

2.4.1. System description

The numerical scheme has been applied to simulate the experimental system of Tang & Gomez (1994), whose parameters are provided in Table 1. This system was previously simulated under the assumption of still air by Grifoll & Rosell-Llompart (2012).

This spray is comprised of non-evaporating primary and satellite droplets. The primary droplet size distribution is the experimental histogram provided by Tang & Gomez (1994), while the satellite droplet distribution is assumed to be log-normal, also based on their data. The computation for droplet charge (q) for both primary and satellite droplets is

based on a single functional dependence of charge-to-mass ratio (ξ) with droplet diameter (d):

$$\xi = ad^b \tag{18}$$

Details on the goodness of the two parameters a and b can be found in Gamero-Castano (2008) and Hai-Bin Tang et al. (2011). For the present spray configuration these parameters were calculated to be $a = 6.13\times10^{-9}$ Cm$^{1.5}$/kg and $b = -1.5$. These values are chosen to be consistent with the report of Tang & Gomez (1994), who find an average charge density of the primary droplets equal to 22.5 C/m^3, and a charge-to-mass ratio dependence with the average diameters for the primary and the satellite droplets given by:

$$\frac{\bar{\xi}_p}{\bar{\xi}_s} = \left(\frac{\bar{d}_p}{\bar{d}_s}\right)^{-1.5} \tag{19}$$

The external electrical field has been calculated by solving Laplace's equation for the electrostatic potential ϕ in the region between the capillary tube and the counterplate, in cylindrical coordinates, using a very fine non-homogeneous grid. The boundary conditions are $\phi = \Phi_0$ at the capillary tube and Taylor cone surfaces; $\phi = 0$ V at the plate, $\partial\phi/\partial z = 0$ at $z = -9H$, and $\partial\phi/\partial r = 0$ at $r = 10H$.

Taking the largest droplet velocity in the system as equal to the jet velocity, we can estimate an upper bound of the Reynolds number, which is 27 for an average droplet moving in still air. This value is well within the range of application of Eq. (3).

Table 2.1. System configuration*

Parameter (units)	Symbol	Value
Capillary-to-plate separation (m)	H	0.03
Capillary tube OD (μm)	D_c	450
Droplet emission point (cm)	z_e	0.24
Count mean diameter for primary droplets (μm)	$\bar{d}_p$	32.3

Coefficient of variation of primary droplets' diameter	$SD_p/\bar{d}_p$	0.06
Count mean diameter for satellite droplets (μm)	$\bar{d}_s$	9.96
Coefficient of variation of satellite droplets' diameter	$SD_s/\bar{d}_s$	0.25
Capillary potential (V)	Φ_0	5000
Liquid flow rate (cc/h)	Q	10

*From Tang & Gomez (1994)

2.4.2. Selection of kernel width

Finding the steady state solution to the governing equations requires a smooth reactive drag force field, since the streamfunction-vorticity formulation uses the spatial derivatives of such force field. Initially we tried computing the reactive drag force density by simply averaging the contributions from droplets present within given control volumes. However, the number of system realizations needed to get a smooth force field became prohibitive. Instead, we have tested the effect of various Gaussian kernel widths (σ) on the smoothing of the ensemble averaged reactive drag force (**d**), as explained in *Section 2.3.1.3.* We have found that 3000 is a practical number of system realizations (N_R) in this system. Such realizations (independent snapshots) were selected at equally spaced times within the period $0.1 < t < 0.7$ s, in which the system was found to be under steady state (following the criterion of Grifoll & Rosell-Llompart, 2012).

Fig.2.3 shows the effect of the Gaussian kernel width (σ) on the axial component of the reactive force density along the centerline. These curves are smooth near the droplet emission point between z_e (0.24 cm) and several mm downstream. But they display increasing noisiness further downstream. This noise grows in amplitude for the smaller values of σ, and is due to statistical under-sampling in regions of the spray where the number density is so low that Eq. (17) is not fulfilled. In the emission point region, the different curves do not coincide, nor do they show an asymptotic trend. This effect is due to the use of kernel sizes which are wider than the spray in this region (shown later). Indeed, near to the emission point the swarm of droplet centers cluster tightly together

around the centerline, within a radius that is smaller than the average primary droplet diameter ($\bar{d}_p$). A choice of kernel width much smaller than $\bar{d}_p$ would lead to an asymptotic **d**(x, y, z) function, provided N_R was large enough. However, such **d** would have no physical meaning because the drag force is transferred from the droplet phase to the gas phase at the length scale defined by the radius of the droplet-air interface (droplet radius) rather than at significantly finer scales.

In order to avoid the large fluctuations found in some of the force density curves of Fig. 3, we have used a combination of kernels in different regions, as summarized in *Table 2.2*. In the region near the emission point we have chosen a kernel width of approximately 2 primary mean droplet diameters (σ = 75 μm) (*Section 2.1.3*). In regions far away from the emission point, where the spray becomes more dilute, the kernel widths have been increased as given in *Table 2.2*.

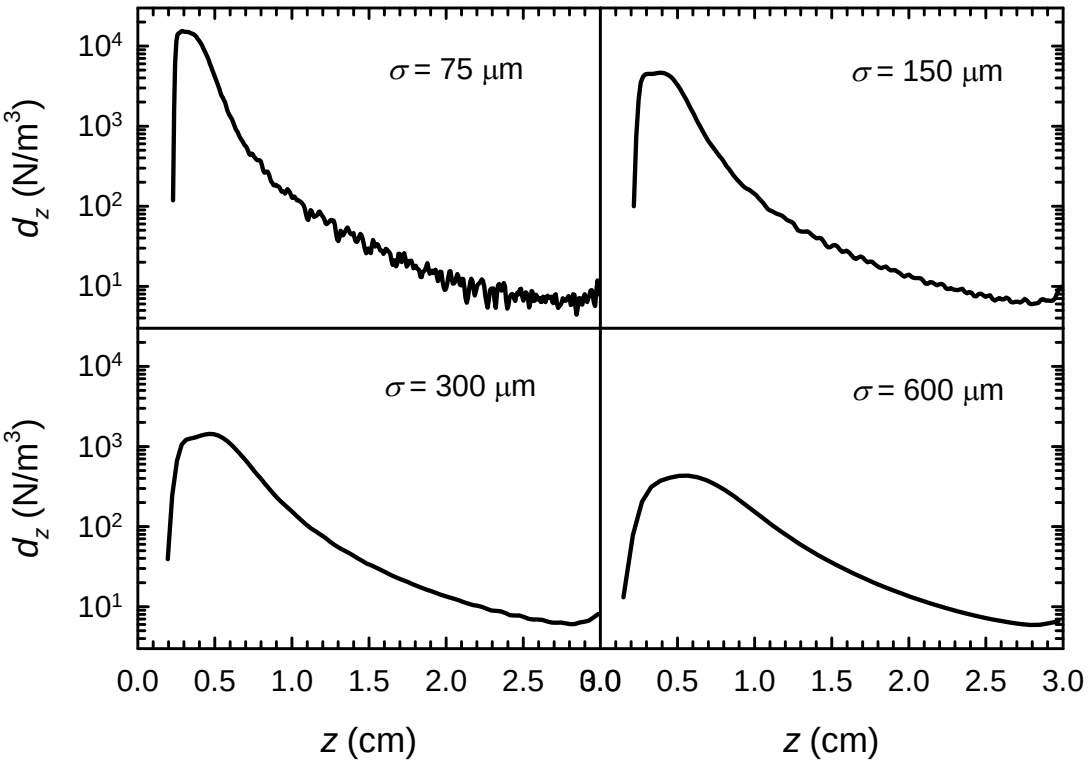

Fig. 2.3. Reactive drag force computed along the axis for different kernel widths.

Table 2.2. Characteristics of the tested kernels.

Kernel size, σ (μm)	Axial range of use (cm)
75	0.0 – 0.6
150	0.6 – 1.0
300	1.0 – 1.5
600	1.5 – 3.0

2.4.3. System simulation

The streamlines for steady-state induced air flow on attaining convergence after five global iterations are shown in *Fig.2.4a*, superimposed on a snapshot of the simulated spray system, also in steady state. *Figure 2.4b* shows another snapshot of the same system, however obtained assuming still air. In both of these simulations the model predicts the segregation of droplets experimentally observed by Tang & Gomez (1994), whereby a shroud of satellite droplets forms around a core of primary droplets. The airflow streamlines of *Fig. 2.4a* show the formation of a jet-like structure. The flow impinges onto the counterplate wherefrom it develops a wall jet boundary layer.

These airflow computations were performed using a non-uniform grid of 193×252 cells extending 10H×10H (Fig. 1). The smallest radial grid size corresponds to $d_{jet}/2$ at the centerline, whereas the smallest axial grid size is 45 μm both at the counterplate and at the capillary tube tip. Grid independency was tested using a double refined grid (386×504 cells). The maximum difference in velocity field between the two solutions was found to be 5.7% at the axis (z = 0.25 cm), and the average variation was 0.12% for the entire flow domain.

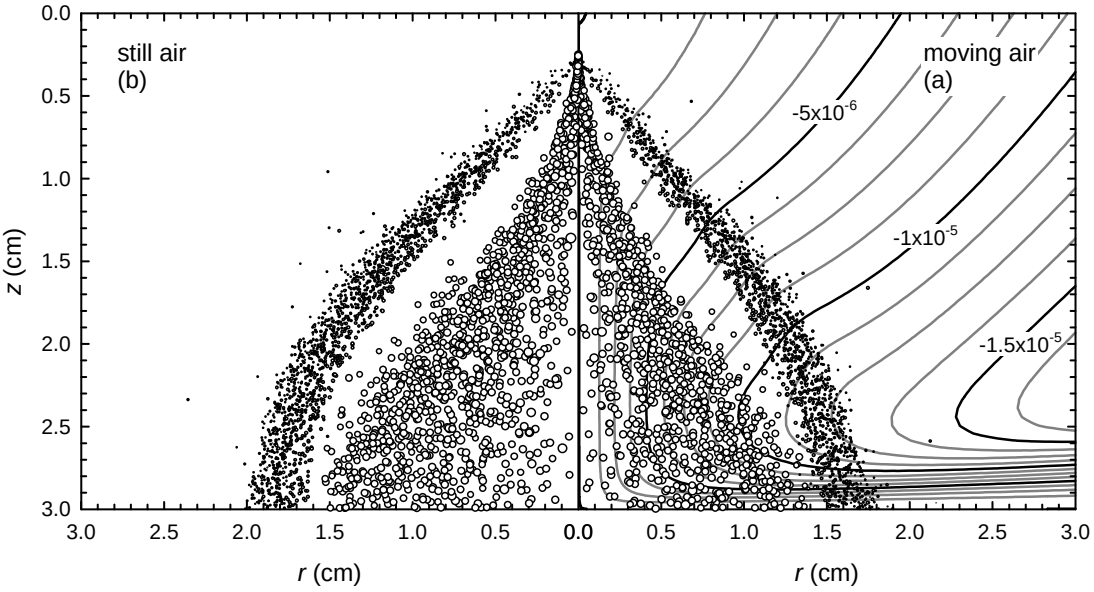

Fig. 2.4. Spray snapshots projected on *rz* plane for (a) simulation with moving air, including the streamlines of the induced air flow, and (b) simulation with still air. The circles diameters are proportional to the actual droplet diameters.

The radial profiles of the axial and radial air velocity components (*Figs. 2.5a, b*) show that high air velocities occur mainly in a region close to the spray axis. *Fig. 2.5a* shows that the axial velocity attains its maximum value at the axis near the emission point. At all axial positions, the axial velocity decays radially from a maximum value at the axis, and is below 0.1 m/s for $r > 0.8$ cm. The inward (negative) radial velocity found at $z = 0.5$ and 1.5 cm (*Fig. 2.5b*) is due to the air entrainment effect (see *Fig.2.4*). When the counterplate is approached (curve for $z = 2.5$ cm) the radial velocity increases as the air spreads radially out forming a wall jet like pattern. The humps present in all these velocity profiles correlate to the presence of the primary and satellite droplet plumes.

The observed radial drop in axial velocity shown in *Fig. 2.5a* is consistent both with the previous experimental determinations of centerline air velocities, and with the conclusions from various radially-averaged conservation balances, that were mentioned earlier in the Introduction.

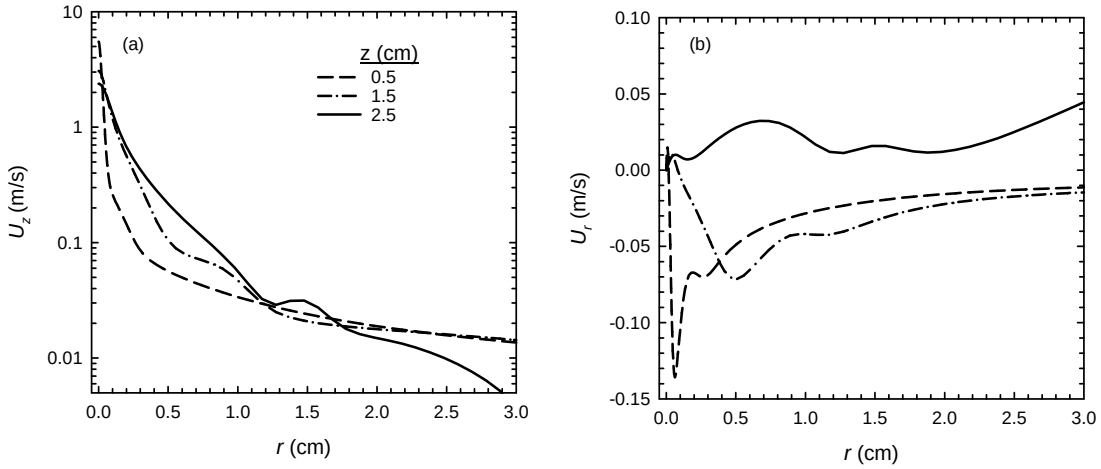

Fig. 2.5. Air velocity at various axial positions: (a) axial component, (b) radial component.

Fig. 2.6 graphs the centerline velocity of the air and the droplets obtained in the experiments of Tang & Gomez (1994) and in the present simulations with and without air flow. Droplets velocities simulated when the air is at rest (gray line) significantly underpredict the experimental values. This line displays a monotonous decrease in the *initial spray zone* ($z < 0.8$ cm), unlike the experimental data (squares). On the other hand, the simulations that account for airflow predict air and droplet velocities which are in fair agreement with the experimental data. In the *downstream spray zone* ($z > 0.8$ cm), the simulated air velocity (dashed line) decays slower than the experimental data (circles), overpredicting them.

We should note that had we computed the air velocity fluctuations term $\rho_f \nabla \cdot \overline{(\mathbf{u}'\mathbf{u}')}$ in Eq. (12), a faster decay of the axial air velocity would have been obtained, because this term would enhance the momentum transfer. In numerical simulations of *electric wind* caused by corona discharges by Zhao & Adamiak (2005) this term was also neglected, and a similar overprediction of the axial air velocities was found, with an increasing deviation towards the centerline. Since the radial variation of axial velocity is maximum at the centerline, this is where maximum overprediction of gas velocity would be expected.

To better understand the droplet dynamics along the centerline, it is also helpful to look at the different terms of the droplet momentum equation (Eq. (1)): the inertia term, the drag force, and the electrical force. We have taken all 3000 snapshots and have averaged each of these terms within equal cylindrical slices of radius 0.03 cm centered at the centerline. As shown in *Fig. 2.7*, the drag tends to zero at the emission point because the droplet and air velocities are equal (to the jet velocity, 12.3 m/s). (This behavior is opposite to the case of still air, for which the drag is *maximum* at this position, rather than *minimum*, and the droplet velocity decays with a significant slope; as shown by the grey line in *Fig.2.6*) Initially (near the droplet emission point), the air momentum at the centerline is rapidly transferred to its surroundings due to the action of viscous stresses, causing a rapid drop in air velocity at the centerline (*Fig.2.6*). As a result, the drag force on the droplets (*Fig. 2.7*) suddenly increases; however this change is too short lived to appreciably change the droplet velocity (*Fig. 2.6*). Beyond this initial transition, which ends at about z = 0.4 cm, the air slows down at a much slower rate. Up to this location the inertia term is near zero (*Fig. 2.7*), consistently with a nearly constant droplet velocity in both the simulated and the experimental results (*Fig. 2.6*). Beyond this zone (z > 0.4 cm), the air velocity continues to decrease (*Fig. 2.6*), causing an increase in the drag force (*Fig. 2.7*), and the electrical force starts to decrease. At about z = 0.55 cm, the drag force reaches a maximum when both the droplets and the air slow down at equal rates. Near the counterplate, the air stream is deflected and the axial velocity drops towards zero (*Fig. 2.6*). As a result, the drag force on the droplets is increased (*Fig. 2.7*), though with minimal effect on the droplet velocity (*Fig. 2.6*). These simulations also show that along the axis the droplets do not attain electrophoretic motion (zero inertia).

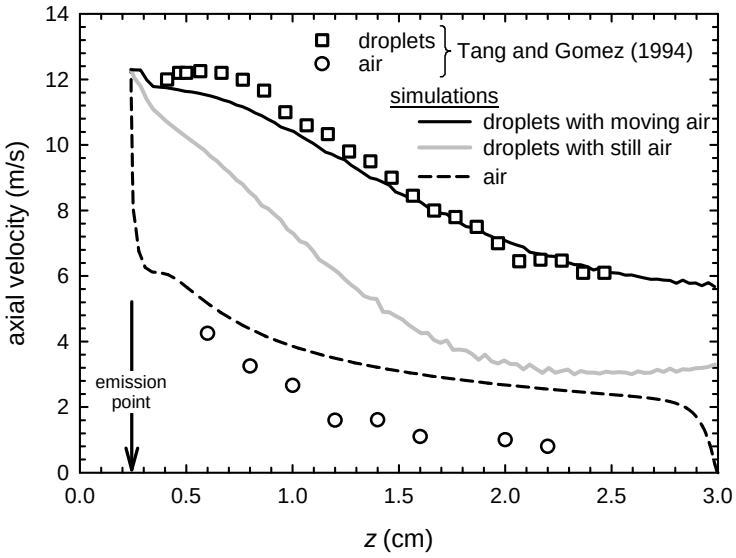

Fig. 2.6. Numerical and experimental values of axial velocities along the centerline for air and droplets.

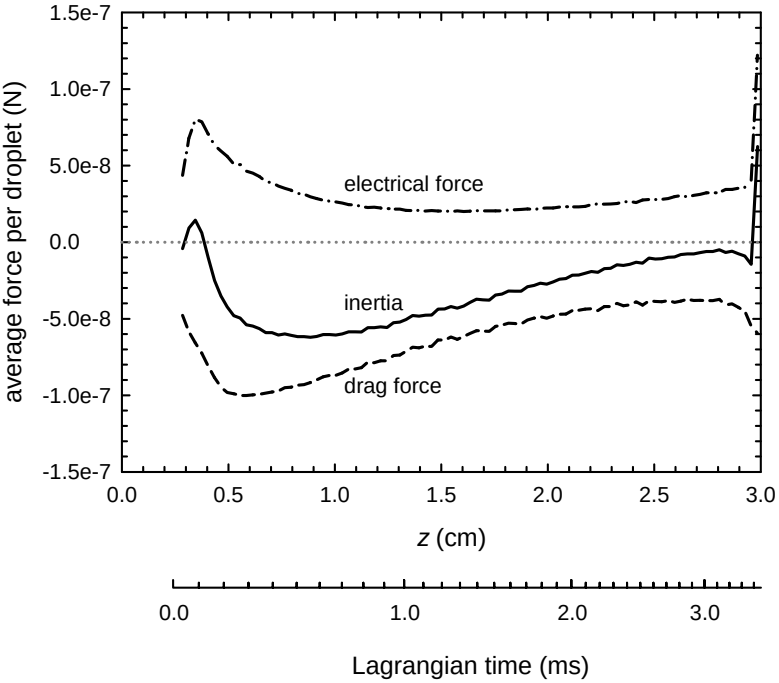

Fig. 2.7. Average electrical forces, drag forces, and inertia sensed by the droplets along the centerline. Secondary abscissa shows the droplet Lagrangian time based on the droplet axial velocity given in *Fig. 2.6*.

Tang & Gomez (1994) also show radial distributions of the number density and average droplet diameter at a constant axial position of z = 1.2 cm. In *Fig. 2.8* we compare these data to our numerical predictions with and without airflow. Volumetric bins of height 250 μm, consistent with the kernel size at this axial location (z = 1.2 cm) were considered for these calculations.

The number density distribution (*Fig. 2.8a*) shows a similar pattern to the experimental data, with a core spray of primary droplets, surrounded by a shroud of satellite droplets. Only when the model includes airflow, the number density near the centerline increases to a maximum, in qualitative agreement with the experimental data. However, a disagreement in number density is found close to the axis, within a region of radius ~1 mm. This disagreement could be the result of two causes. First, the actual charge-to-mass ratio for the largest droplets might be higher than as defined in Eq. (19). If so, the actual particles would be expected to expand radially faster than predicted by the present model, leading to a reduced number density. Second, because the model neglects the fluctuation term $\rho_f \nabla \cdot \left(\overline{\mathbf{u}'\mathbf{u}'} \right)$ (as discussed earlier), it may lead to overprediction of the air axial velocity at the centerline, resulting in a shorter Lagrangian time for the droplets. This would imply lesser expansion by space charge repulsion near the centerline, and an increased number density.

We have quantified the effect on the number density shown in Fig. 8a when increasing the kernel size in the initial axial range, $0 < z < 0.6$ cm (Table 2) from 75 to 150 μm. The effect is minor, with only a 7% decrease in the number density at the centerline (r = 0) which rapidly diminishes to a 1.4% decrease at r = 0.5 mm. However, as argued earlier in the context of *Fig. 2.3*, 75 μm is a more appropriate kernel size for the initial axial range.

On the other hand, the locations of both the primary and satellite droplet plumes show better agreement with the experiments, than the simulations which consider still air. This improvement is the result of two factors. First, the axial motion of the cloud is faster in the presence of airflow. Therefore, the droplets sampled at a fixed z are "younger" (in Lagrangian time) than when airflow is neglected. And a younger spray should have expanded radially less than an older one. Second, the radially converging airflow close to the droplets' emission point reduces the extent of radial expansion (*Fig. 2.4*).

The average diameter profile (*Fig. 2.8b*) also shows better overall agreement with the experimental data when airflow is included than when it is not (except in regions for which the droplet count, shown in *Fig. 2.8a*, is very low).

Initially, we had carried out the simulations assuming a constant charge-to-mass ratio for both primaries and satellite droplets, as done previously by Grifoll & Rosell-Llompart (2012) in absence of airflow. This assumption was consistent with the information provided in Tang & Gomez (1994), but, under the presence of airflow, resulted in *reverse* dependence of local satellite diameter *versus r.* In conclusion, the radial segregation by size of the satellite droplets is sensitive to the functional relationship between charge-to-mass ratio and diameter. By contrast, the assumed relationship given by Eq. (18), which is also consistent with Tang & Gomez (1994), leads to a correct prediction of the segregation effect (*Fig. 2.8b*).

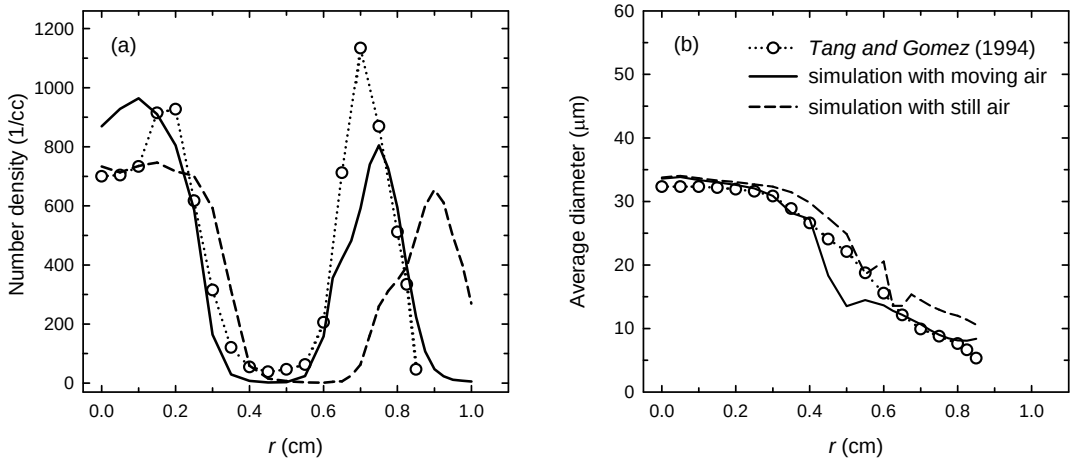

Fig. 2.8. Radial profiles at z =1.2 cm of (a) droplet number density, and of (b) droplet diameter.

Figs. 2.9a, b show the radial distributions of the droplets' axial mass flux at two axial locations (z = 1.2 cm and on the counterplate, i.e. z = 3 cm) for the cases of still air and moving air. The ability to predict the droplet mass flux is of interest to practitioners of electrospray deposition who make thin films and coatings. In *Figs. 2.9a* and *b*, the contribution from the satellite droplets to the mass flux is extremely small, as can be confirmed by comparing *Fig. 2.9a* with *Fig. 2.8a*, and *2.9b* with *2.4* . The effect of the

induced airflow is to raise the mass flux near the center and reduce the plume width. The ratio of mass flux at the centerline between the cases of moving and still air is 2.2 at z = 1.2 cm, and 2.6 at z = 3.0 cm. This effect is the result of the aforementioned causes of inwardly radial airflow and reduction of Lagrangian time available for cloud expansion. An indication of reduced residence time of the plume in the presence of airflow is the reduction in average number of primary droplets in the plume from 1125 in still air to 904 in moving air, and in the average number of satellites from 1755 to 1656. It should be noted that close to the centerline, the flux may be overpredicted since, while the droplet velocity closely agrees with the experiments (*Fig. 2.6*), the centerline number density is overpredicted (*Fig. 2.8a*).

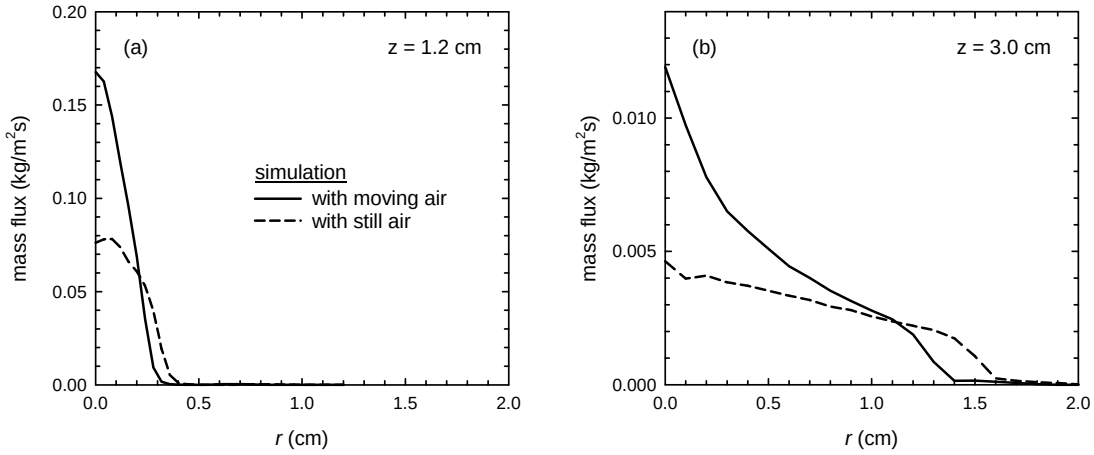

Fig. 2.9. Comparison of mass flux assuming still or moving air at (a) z = 1.2 cm and (b) z = 3.0 cm.

2.5. Conclusions

The air flow induced by droplet motion has been included into a Lagrangian model of electrosprays. Steady state solutions for air flow and droplet dynamics were sought iteratively in a fully coupled computational scheme. Detailed simulations have been performed on an electrospray plume which was experimentally characterized by Tang &

Gomez (1994). Results show that including air motion in the simulations modifies the droplet trajectories significantly. Radial profiles of number density, and of local average droplet diameter, and centerline droplet velocities show better agreement with the experimental data when airflow is taken into account. Significant air entrainment towards the spray axis is observed near the droplet generation region, which develops into a jet like structure that impinges onto the counterplate. The droplets mass flux radial distribution is particularly sensitive to the air entrainment, which results in a steep increase near the spray axis.

In order to resolve the reactive force on the air by the droplets while using a practical number of independent system realizations, it is necessary to use a filter. In the present simulations, with 3000 ensemble-averaged realizations, we have used a range of Gaussian filters differing in kernel width at different axial locations. At the denser spray regions close to the droplet emission point, the kernel size should neither be much wider nor much smaller than the average droplet diameter. Further downstream, where the droplet number density decreases, a wider kernel width has been used in order to suppress the fluctuations in the reactive force density.

2.6. References

Abraham, F. F. (1970). Functional dependence of drag coefficient of a sphere on Reynolds number. *Physics of Fluids, 13*, 2194-2195.

Apte, S.V., Mahesh, K., & Lundgren, T. (2008). Accounting for finite-size effects in simulations of disperse particle-laden flows, *Int. J. Multiphase Flow, 34*, 260-271.

Bock, N., Dargaville, T.R., Woodruff, M.A. (2012). Electrospraying of polymers with therapeutic molecules: State of the art, *Progress in Polymer Science*, *37*, 1510-1551.

Bodnár, E. & Rosell-Llompart, J. (2013). Growth dynamics of granular films produced by electrospray, *J. Coll. Int. Sci.*, submitted.

Deen, N.G., van Sint Annaland, M., Kuipers, J. A. M. (2004). Multi-scale modeling of dispersed gas-liquid two-phase flow. *Chem. Eng. Sci., 5*9, 1853-1861.

Deng, W., & Gomez, A. (2007). Influence of space charge on the scale-up of multiplexed electrosprays. *J. Aeros. Sci., 38,* 1062-1078.

Deshpande, M.D., & Vaishnav, R.N. (1982). Submerged laminar jet impingement on a plane. *J. Fluid Mech., 114*, 213-236.

Fenn, J.B., Mann, M., Meng, C.K., Wong, S.F., & Whitehouse, C.M. (1989). Electrospray ionization for mass spectrometry of large biomolecules, *Science, 246* (4926), 64-71.

Fenn, J. B. (2003). Electrospray wings for molecular elephants (Nobel lecture), *Angew. Chem.-Int. Ed., 42*(33): 3871-3894.

Finn, J., Shams, E., & Apte, S. V. (2011). Modeling and simulation of multiple bubble entrainment and interactions with two dimensional vortical flows. *Phys. Fluids, 23*, 023301 (1-20).

Gamero-Castano, M. (2008). The structure of electrospray beams in vacuum. *J. Fluid Mech.*, *604*, 339-368.

Gañan-Calvo, A. M., Lasheras, J.C., Davila, J., & Barrero, A. (1994). The electrostatic spray emitted from an electrified conical meniscus. *J. Aeros. Sci., 25*, 1121-1142.

Gosman, A. D., Pun, W. M., Runchal, A. K., Spalding, D. B., & Wolfshtein, M. (1969). *Heat and mass transfer in recirculating flows*. Academic Press Inc.: London.

Grifoll, J. & Rosell-Llompart, J. (2012). Efficient Lagrangian simulation of electrospray droplets dynamics. *J. Aeros. Sci., 47*, 78-93.

Hai-Bin Tang, Chao-Jin Qin & Yu Liu. (2011). Characterization of colloid thruster beams and plumes. *J. Aeros. Sci., 42,* 114-126.

Hartman, R. P. A., Borra, J. P. , Brunner, D. J. , Marijnissen, J. C. M., & Scarlett, B. (1999). The evolution of electrohydrodynamic sprays produced in the cone-jet mode, a physical model. *J. Electrostat.*, *47*, 143-170.

Higuera, F. J. (2012). Eulerian model of a dilute spray of charged droplets. *J. Aeros. Sci., 48,* 34-45.

Jaworek, A. (2007). Electrospray droplet sources for thin film deposition. *J. Mater. Sci., 42,* 266-297.

Jaworek, A. & Sobczyk, A.T. (2008). Electrospraying route to nanotechnology: An overview. *J. Electrostat., 66*, 197-219.

Jung, J. H., Oh, H., & Kim, S. S. (2010). Numerical simulation of the deposition pattern in multiple electrohydrodynamic spraying. *Powder Technol.*, *198*, 439-444.

Kim, I., Elghobashi, S., Sirignano, W. A. (1993) Three-dimensional flow over two spheres placed side by side. *J. Fluid Mech., 246*, 465-488.

Kitagawa, A., Murai, Y., Yamamoto, F. (2001). Two-way coupling of Eulerian–Lagrangian model for dispersed multiphase flows using filtering functions. *Int. J. Multiphase Flow, 27*, 2129-2153.

Maxey, M.R., & Patel, B.K. (2001). Localized force representations for particles sedimenting in Stokes flow. *Int. J. Multiphase Flow, 27,* 1603-1626.

Oh, H., Kim, K., & Kim, S. (2008). Characterization of deposition patterns produced by twin-nozzle electrospray. *J. Aeros. Sci.*, *39*, 801-813.

Rietveld, I. B., Kobayashi, K., Yamada H., & Matsushige, K. (2006). Electrospray deposition, model, and experiment: Toward general control of film morphology. *J. Phys. Chem. B*, *110*, 23351-23364.

Rosell-Llompart, J. & Fernandez de la Mora., J. (1994). Generation of monodisperse droplets 0.3 to 4 μm in diameter from electrified cone-jets of highly conducting and viscous liquids. *J. Aeros. Sci., 25*, 1093-1119.

Tang, K. & Gomez, A. (1994). On the structure of an electrostatic spray of monodisperse droplets. *Phys. Fluids, 6*, 2317-2332.

Wilhelm, O., Madler, L., & Pratsinis, S. E. (2003). Electrospray evaporation and deposition. *J. Aeros. Sci.*, *34*, 815-836.

Yang, W., Lojewski, B., Wei, Y., & Deng, W. (2012). Interactions and deposition patterns of multiplexed electrosprays. *J. Aerosol Sci., 46,* 20-33.

Zhao, L. & Adamiak, K. (2005). EHD flow in air produced by electric corona discharge in pin–plate configuration. *J. Electrostat.*, *63,* 337-350.

Chapter 3

Chapter 3

Numerical simulations of evaporating electrosprays with Coulomb explosions[b]

3.1 Abstract

The design and optimal operation of electrospray devices can be facilitated with the help of numerical simulations of the relevant phenomena in order to reduce the experimental burden. In this study, mechanistic models for the diverse phenomena have been implemented in numerical codes in order to simulate volatile electrosprays. The overall model includes a Lagrangian description of the droplets dynamics, shrink of droplets due to evaporation and Coulomb explosions, as well as Eulerian descriptions for the gas flow induced by the droplets, the transport of vapor, and the electrical charge leftover by the vanishing droplets. To couple the different physics, the Lagrangian code and the three Eulerian ones were run sequentially, taking the inputs needed for each code from the results of the preceding runs. The Eulerian codes were formulated under steady state, while for the Lagrangian model we take an ensemble average of a steady-state portion of the simulation as representative. After several sequences of simulations, each variable field converged and the overall result was taken as illustrative of the behavior of the electrospray under steady state. This methodology has been applied to three electrospray systems with solvents of different volatility: acetone, methanol and n-heptane. The droplets were injected into the three systems with unimodal and log-normal distributed diameters with mean 8 μm, and a coefficient of variation of 10%. Regions of intense Coulomb explosion events in form of diagonal bands within the spray are well captured. In all three cases, few or no droplets arrive at the counterplate located 3 cm down the capillary nozzle, highlighting the relevance of accounting for evaporation when simulating these systems.

[b]***This chapter will be submitted to Journal of Aerosol Science (2014)***

Nomenclature

Roman letter symbols

$\mathbf{A_i}$	droplet acceleration vector (m^2/s)
$B_{M,neq}$	$\left(= \frac{Y_{S,neq} - Y_G}{1 - Y_{S,neq}} \right)$ non equilibrium Spalding transfer number for mass
C_c	$\left(= 1 + \frac{\lambda}{d}\left[2.514 + 0.8 \exp\left(\frac{-0.55d}{\lambda} \right) \right] \right)$ Cunningham slip correction factor
C_D	droplet drag coefficient
C_L	specific heat capacity of liquid
$C_{p,G}$	specific heat capacity of air at atmospheric pressure
C_V	vapor concentration density (mol/m^3)
C_q	*residual charge* concentration density (C/m^3)
d	ensemble averaged reactive drag force density (N/m^3)
D	instantaneous reactive drag force density (N/m^3)
D_c	capillary tube outer diameter (m)
d_i	diameter of *i*-th droplet (m)
d_{jet}	electrospray jet diameter (m)
dt	time interval (s)
$\overline{d}_p$	count mean primary droplet diameter (m)
$\overline{d}_s$	count mean satellite droplet diameter (m)
$\mathbf{E_{ext}}$	external electrical field (V/m)
f_l	$\left(= \frac{\beta}{e^{\beta} - 1} \right)$ correction factor to heat transfer (accounting for evaporation)
$\mathbf{F_i}$	drag force acting on droplet *i* (N)

$\mathbf{F_{elec,i}}$ electric force acting on droplet *i* (N)

H capillary tube tip to counterplate distance (m)

H_M $\left(= \ln\left[1 + B_{M,neq}\right]\right)$ mass transfer potential

K electrical mobility of *residual charge* (m^2/V-s)

L_V latent heat of vaporization

m_d mass of droplet (kg)

$\dot{m}_d$ droplet mass transfer rate (kg/s)

N_P number of progeny droplets

Nu Nusselt number

Pr_G $\left(= \frac{\mu_g C_{p,G}}{\lambda_g} \right)$ Prandtl number for gasflow

q_i electrical charge of droplet *i* (C)

q_R electrical charge of a droplet at Rayleigh limit (C)

Q liquid flow rate (m^3/s)

r polar coordinate (m)

Re_i $\left(= \frac{\rho_f \left|\mathbf{u} - \mathbf{V_i}\right| d_i}{\mu} \right)$ Reynolds number

$\mathbf{R_i}$ (= $[x_i, y_i, z_i]$) position vector of *i*-th droplet (m)

$\mathbf{R_I}$ (= $[x_i, y_i, 2H - z_i]$) position vector of image of *i*-th droplet on counterplate (m)

$\mathbf{R_{ij}}$ (= $\mathbf{R_i} - \mathbf{R_j}$) displacement between the position vectors of droplets *i* and *j* (m)

$\mathbf{R_{iJ}}$ (= $\mathbf{R_i} - \mathbf{R_J}$) displacement between the position vectors from the image of droplet *j* on the counterplate to droplet *i* (m)

Sc_G Schmidt number for gasflow

Sh Sherwood number

T_d temperature of the droplet (K)

T_G temperature of the gas (K)

$\mathbf{u}$ mean gas velocity vector (m/s)

$\mathbf{u_q}$ (=K$\mathbf{E}$+$\mathbf{u}$) residual charge velocity vector (m/s)

$\mathbf{U}$ instantaneous gas velocity vector (m/s)

Ur, Uz radial and axial components of mean gas velocity vector (m/s)

t time (s)

V volume of the spray (m^3)

$\mathbf{V_i}$ velocity vector for droplet i (m/s)

V_{jet} electrospray jet velocity (m/s)

$\mathbf{x}$ (=[x,y,z]) position vector (m)

Y_G free stream vapor mass fraction

$Y_{S,neq}$ non-equilibrium vapor mass fraction at droplet surface

z_e droplet emission point (m)

Greek letter symbols

α $\left(= \left[\frac{q}{q_R} \right]_{progeny} \right)$ Ratio of charge limit for progenies

β $\left(= \frac{3 \, \mathrm{Pr}_G \, \tau_d}{2} \left[\frac{\dot{m}_d}{m_d} \right] \right)$ non dimensional evaporation parameter accounting for blowing effect

γ surface tension of liquid (N/m)

Γ diffusivity of liquid species in air (m^2/s)

ε_0	electrical permittivity of vacuum (8.854×10^{-12} C/V·m)
ξ	droplet charge to mass ratio (C/kg)
λ	mean free path of air molecules (m)
μ_g	dynamic viscosity of surrounding gas (kg/m·s)
ϕ	electrostatic potential (V)
Φ_0	electrostatic potential at the capillary tube (V)
ρ_d	density of drop liquid (kg/m^3)
ρ_f	density of surrounding gas (kg/m^3)
θ_1	$\left(=\frac{C_{p,G}}{C_L}\right)$ ratio of specific heat capacities
τ_d	$\left(=\frac{d^2\rho_d}{18\mu_g}\right)$ droplet time constant for Stokes flow

Acronyms

CFD	Computational Fluid Dynamics
CVFD	Control Volume Finite Difference
CSC	Continuous Space Charge
OD	Outerdiameter

3.2 Introduction

Electrosprays are constituted of highly charged micro or nano droplets which are created by the action of electrostatic forces on a liquid. The droplets hence generated are transported under the combined influence of the electrostatic gradient between the spray needle and counterplate, the interaction with the spray charge and the aerodynamic drag force. Some important applications of such sprays are in electrospray ionization mass spectrometry (ESI-MS) (Fenn et al, 1989), particle synthesis (Jaworek & Sobczyk, 2008; Bock et al, 2012), and thin film deposition (Jaworek, 2007). Droplet evaporation is a critical aspect aimed at producing the desired result in these applications. For example, the extent of droplet evaporation determines the variety of product morphologies that can be

achieved via electrospray deposition (Rietveld et al, 2006, Bodnár & Rosell-Llompart, 2013).

Owing to the considerable effort required to setup an experimental electrospray system to study its various influencing parameters, and the limitations associated with the measurement techniques, numerical simulations are a powerful approach in the design and analysis of electrosprays. Given the importance of droplet evaporation in electrospray applications, the numerical simulations of many practical electrospray systems should include this phenomenon. However, most of the available numerical simulation models on electrosprays have considered non-volatile droplets. Thus, following the original Lagrangian description of droplet dynamics in an electrospray by Gañan-Calvo et al. (1994), a number of non-volatile electrospray systems were numerically simulated by different authors, viz., Hartman et al. (1999), Oh et al. (2008), Jung et al. (2010), Yang et al. (2012) and Grifoll & Rosell-Llompart (2012, 2014). Distinct description of an electrospray system through an Eulerian model by Higuera (2012) has also assumed the spray to be non-volatile.

The few numerical works that have considered volatile electrosprays are the studies by Wilhelm et. al (2003) and Sen et. al (2011). In both of these, the spray system was assumed to evaporate against zero solvent background vapor concentration in still ambient conditions, wherein the droplet fission was considered. No account for including the airflow was done, and under this assumption diffusion alone contributed to vapor transport. Furthermore, any corrections in the electrostatic field due to charges left behind by the fully evaporating droplets were not described in these works.

Wilhelm et. al. (2003) simulated the transport, evaporation and deposition of n-butanol electrospray containing yttrium and zirconium salts on a heated substrate. They combined the Lagrangian droplet dynamics model with a simplified Abramzon-Sirignano evaporation model (1989); after performing an order of magnitude calculation to rule out any significant contribution from air entrainment. A trial and error approach was followed to identify the vapor background concentration which closely fit to the deposited salt concentration.

Sen A.K et. al (2011) assumed monodisperse electrospray in the Lagrangian framework experiencing droplet fission in a stationary medium. A simple kinetic evaporation model, more suitable for evaporation of sub-micron drops in stagnant ambient

conditions, was used in their simulations. However, while mentioning the discrepancies in droplet velocities, the authors suggestively acknowledged that it could be due to the fact that the effect of air entrainment into the spray has been overlooked in their simulations.

While formulating a complete numerical framework for a volatile electrospray, one should consider the aspects of ambient gas conditions (e.g. gasflow dynamics, presence of temperature gradients, vapor saturation level), Coulomb explosions on droplets reaching their Rayleigh limit, production and transport of solvent vapor, precipitation of solutes within droplets, transport of charged residual particle impurities and (or) ions generated by ion desorption or by the charge residue mechanism, etc. These aspects can influence the rate of droplet evaporation, the droplet dynamics and hence the electric field. Since gas motion can be a significant factor in droplet evaporation, rigorous numerical framework of volatile electrosprays should also include the influence of the gas flow induced by the droplet motion.

Here we couple various numerical models to attain the description of the behaviour of evaporating electrospray systems undergoing Coulomb explosions, additionally solving for the induced gasflow; the transport equations for vapor and for charges left behind upon complete droplet evaporation. Coupled are the Continuous Space Charge approximation model (Grifoll and Rosell-Llompart, 2014) for the Lagrangian droplet dynamics, an Eulerian vorticity-streamfunction method to describe the induced gas flow (Arumugham-Achari et. al., 2013), and a non-equilibrium Langmuir-Knudsen evaporation model (Miller et. al., 1998) for sprays. This methodology has been applied to compare three electrospray systems with solvents of different volatility: acetone, methanol and n-heptane.

3.3 Mathematical model and methodology

In a volatile electrospray system multiple and complex phenomena interact with each other. In order to simulate them, we have developed separate models for each phenomenon. The numerical codes into which each of those models is implemented are run sequentially. A sequence of runs that includes the simulations of all phenomena is called a stage. When simulating a phenomenon, the results of the simulation of the preceding phenomena are taken as inputs. The numerical method solves for pseudo-steady state solutions for the droplets dynamics, and the steady state solution for gas, vapor and

charge transports. The motion of evaporating droplets under electric forces in moving gas is simulated by a 3D Lagrangian particle tracking model. The droplet-induced pseudo-steady gas flow, the transport of vapor and charges from complete droplet evaporation are simulated by 2D axisymmetric Eulerian models. Since the volume fraction of the droplet phase is much smaller than unity, the dilute aerosol approximation has been adopted. A final steady state configuration for the volatile electrospray system is obtained when numerical convergence is obtained for successive stages in all these frameworks.

3.3.1. Governing equations

3.3.1.1 Lagrangian particle dynamics

The 3D Lagrangian droplet dynamics simulations are based on the model first proposed by Gañan-Calvo et al (1994). The electrospray system is considered to be made of electrostatically interacting droplets considered to be point particles for which the mutual aerodynamic interactions are not considered. The droplets experience drag from the surrounding gas, and electrical force from the electrodes and spray charges. Following these assumptions, the droplet dynamics are described by Newton's second law through the equations:

$$\frac{d\,\mathbf{R}_i}{d\,t} = \mathbf{V}_i \tag{1}$$

$$\frac{\pi}{6} d_i^3 \rho_d \frac{d\,\mathbf{V}_i}{d\,t} = \mathbf{F}_i + \mathbf{F}_{\mathbf{elec},i} \tag{2}$$

Equations (1) and (2) determine the trajectory of each droplet i from the emission point to the counterplate, where $\mathbf{F}_i$ and $\mathbf{F}_{\mathbf{elec},i}$ are the drag and electric forces acting on droplet i, which are given by:

$$\mathbf{F}_i = C_D \frac{\pi}{8} d_i^2 \rho_f \left(\mathbf{u} - \mathbf{V}_i\right)\left|\mathbf{u} - \mathbf{V}_i\right| \tag{3}$$

$$\mathbf{F}_{\mathbf{elec},i} = q_i\, \mathbf{E}\left(\mathbf{R}_i\right) \tag{4}$$

For calculating the electric force as in equation (4) we follow the *Continuous Charge submodel* of Grifoll and Rosell-Llompart (2014). This technique is a modification to the classical Lagrangian method, in which the sum of droplet-to-droplet interactions is

replaced by the mean electric field due to the droplets space charge which is solved using Gauss's law (Poisson's equation). This method considerably brings down the computational time needed for calculating the electrical forces in systems with large number of droplets. The continuous charge density appearing in Gauss's law is estimated considering the charge carried by the droplets present in elemental volumes defined in a 2D cylindrical coordinate system aligned with the spray.

Grifoll and Rosell-Llompart (2014) show that the procedure is not applicable in two regions: close to the emission point (where the droplets move almost in a row), and close to the spray axis (when the neighboring droplets create fluctuations in the radial electric field that greatly exceed the time averaged radial electric field). To overcome this drawback, the system is split into two regions, R1 and R2, in which different methods of computing the electrical forces on a droplet are considered. Region R1 is defined as a cylinder centered on the system axis, and region R2 as the space outside R1. The electrical field acting on a droplet in R1 is obtained by adding the continuous field due to the droplets in R2 (and the electrodes and boundaries), solved using Poisson's equation, plus all the individual fields due to the other droplets in R1. Whereas the electrical field experienced by a droplet in R2 is obtained by solving Poisson's equation for the whole spray charge plume (with appropriate boundary conditions).

3.3.1.2. Evaporation of droplets and Coulomb explosions

A number of droplet evaporation models have been developed to simulate droplet evaporation in sprays. Comprehensive reviews of such models can be found in the works of Sazhin (2005, 2006), for high temperature applications like spray combustion, and of Miller *et al*. (1998) for general droplet gas-liquid flow simulations. Miller et al. (1998) show that all the models, including the classic so called d^2 law, perform equally well in low pressure and low temperature applications. However, they conclude that the Langmuir-Knudsen models have the ability to perform better over a wider range of temperature and pressure conditions. Jakubczyk *et al*. (2012) studied the range of applicability of classic d^2 law in the evaporation of droplets in the atmosphere, and concluded that considerable departure from the classic law can be encountered by the influence of impurities in liquids, or by surface tension and kinetic effects for small droplets. Among the available evaporation models, here we have considered the

convective Langmuir-Knudsen non-equilibrium model (M7 of Miller *et al.*, 1998) as it offers various advantages over others: It is simpler to implement, considers Stephan flow, rarefaction (kinetic) effects important in the evaporation of small droplets, and needs no iterations, unlike the popular Abramzon and Sirignano (1989) model. Hence it is computationally efficient and applicable for simulating sprays involving a large number of small droplets which are in relative motion with respect to the host gas. The Kelvin effect, which is prominent only for submicron ranges (Hinds, 1999), has not been considered. On neglecting the non-uniform internal temperature effects (i.e., assuming infinite liquid thermal conductivity), the governing equations of this droplet evaporation model can be summarized as follows:

$$\frac{d\,T_d}{d\,t} = \frac{f_1\,Nu}{3\,Pr_G}\frac{\theta_1}{\tau_d}\left(T_G - T_d\right) + \frac{L_V}{C_L}\frac{\dot{m}_d}{m_d} \tag{5}$$

$$\frac{dm_d}{dt} = -\frac{Sh}{3Sc_G}\left(\frac{m_d}{\tau_d}\right)H_M \tag{6}$$

where the Frössling correlations for heat and mass transfer have been used to estimate the Nusselt and Sherwood numbers as

$$Nu = 2 + 0.552\,Re_d^{1/2}\,Pr_G^{1/3} \tag{7}$$

$$Sh = 2 + 0.552\,Re_d^{1/2}\,Sc_G^{1/3} \tag{8}$$

As the droplets evaporate, their charge to mass ratio increases, and are assumed to undergo Coulomb explosions on reaching the Rayleigh limit which is given by

$$q = q_R = \sqrt{\left(8\pi^2\varepsilon_o\gamma d^3\right)} \tag{9}$$

The mass, charge and number of progenies discharged from the parent droplets through such an explosion, have a wide range of values been reported. Such data from various literatures are summarized in *Table 3.1*.

Table 3.1 Summary of data reported in literature on mass and charge loss through Coulomb explosions

Reference	Solvent	Drop diameter range (microns)	Instability onset range % of q_R	Fractional mass loss $\Delta m/m$ (%)	Fractional charge loss $\Delta q/q$ (%)
Smith et al (2002)	Water	10-40	90	NA	20-40
	Methanol	10-40	110	NA	15-20
	acetonitrile	10-40	100	NA	15-20
Grim & Beauchamp (2002)	n-heptane	35-45	101	NA	19
	n-octane	35-60	87	NA	17
	p-xylene	10-40	89	NA (<2)	17
Gomez & Tang (1994)	heptane	20-100	70		
Taflin (1989)	low vapor pressure oils	4-20	80±5	2	10-15
Richardson et al (1989)	dioctyl phtalate		93±9	2.3	15-50
	sulphuric acid		94.5±10.5	0.1	41.1-57.7
Schweizer et al (1971)	n-octanol	15-40	100±4	5	23
Davis&Bridges (1993)	1-dodecanol	10-20	85±5	1.6-2.35	
Hunter & Ray (2009)	diethylphthalate (pure)		96	1.83-2.73	15.9-25.7
	diethylphthalate (increased solute concentration)		96	0.05	35
K.-Y. Li et al (2005)	hexadecane	5-25	96±6	1.11-1.5	13-17.6
	diethylene glycol		104±7	< 0.03	35.7-39.7
	triethylene glycol		100±5	< 0.03	35.8-76.4
	diethylphthalate		97±6	1.83-2.73	15.9-25.7
	diethylphthalate	26.468	99.8	2.86	23.1
Grim & Beau. (2005)	Methanol	225	100	0.79	13
Tang & Smith (1999)	generic fluid	NA	100	2	15

* NA- data not available

While in most of the studies the limitation in instrument accuracy prevents fractional mass loss detection below 2%, most of them give an account of the fractional charge loss through Coulomb explosions. Davies & Bridges (1993) agrees with the analysis of Roth & Kelly (1983) that in their experimental 1-dodecanol spray, fission generated around 4-5 progenies for 2% mass loss; 2-3 for 1% mass loss, which in turn kept the progeny charges below their Rayleigh limit. K.-Y. Li et al (2005), through Lorentz-Mie scattering on pure single droplet break-ups detected progressively at various diameter en route of full evaporation, observed that few large progenies with 60-100% of their Rayleigh limit were created by low conductivity liquids. According to them, thousands of small progenies of less than 0.03% mass fraction were generated by the droplet fission for high conductivity liquids. Hunter & Ray (2009), through Gibbs free energy analysis conclude that in general it is numerically justified to assume that a Coloumb fission creates identical progenies that can carry 50-100% charge of their Rayleigh limits. Tang & Smith (1999), calculates that 4 progenies are generated through the disruption having 10% of parent drop diameter, while the parent droplet loses 15% of its charge.

Hence from the above studies we summarize that the fractional mass ($\Delta m/m$) and charge loss ($\Delta q/q$) on Coulomb explosions have dependence on the solvent physical properties like electrical conductivity and surface tension. A higher conductivity can result in smaller mass loss and higher charge loss. In general, the observed ranges for the parameters are:

$$\frac{\Delta m}{m} \sim (< 0.03\% - 2\%) \tag{10}$$

$$\frac{\Delta q}{q} \sim (20\% - 70\%) \tag{11}$$

$$N_p \sim \text{few to 1000's} \tag{12}$$

where N_p is the number of progenies resulted from a single explosion.

On evaporation and subsequent Coulomb explosions the droplets and their progenies may produce ions by field desorption, or can become fully evaporated, leaving behind charged precipitates (solid residues) or molecular ion residues which get transported within the system by virtue of their electrical mobility (Fenn et al., 1996). Such charged species are collectively called *residual charges* hereafter.

3.3.1.3. Gasflow dynamics and transport of vapor and charge

The body force impelling the gas flow is the reactive drag force due to the motions both of droplets and of *residual charges*. Therefore, the gas motion (assumed isothermal) is governed by the continuity equation (assuming incompressible gas flow) and the Navier-Stokes equations including such drag force:

$$\nabla \cdot \mathbf{u} = 0 \tag{13}$$

$$\rho_f \mathbf{u} \cdot \nabla \mathbf{u} = -\nabla p + \mu \nabla^2 \mathbf{u} + \mathbf{d} \tag{14}$$

where **u**, p and **d** are the components of gasflow velocity, pressure and reactive drag force density. The 2D Eulerian gasflow equations were formulated based on the vorticity-streamfunction method, and were solved through the Control Volume Finite Difference (CVFD) discretization scheme proposed by Gosman et al. (1969). More details on the solution of induced gasflow in electrosprays are provided by Arumugham-Achari *et al*. (2013).

Under the assumption that the gasflow and hence the vapor transport is steady, the transport equation for electrospray solvent vapor in 2-D axisymmetric cylindrical co-ordinates is

$$u_r \frac{\partial C_V}{\partial r} + u_z \frac{\partial C_V}{\partial z} = \Gamma \left[\frac{1}{r} \frac{\partial}{\partial r} \left(\frac{\partial C_V}{\partial r} \right) + \frac{\partial^2 C_V}{\partial z^2} \right] + S_V \tag{15}$$

where u_r and u_z are the radial and axial components of gas velocity, Γ is the binary diffusion coefficient of vapor in the carrying gas (here *air*), C_V is the vapor concentration density (mol/m^3), and S_V is the vapor volumetric generation rate (mol/m^3 s).

The transport of *residual charge* is assumed to be described by a steady-state continuous field. It is thus based on the charge conservation equation

$$\nabla \cdot \mathbf{j} = S_q \tag{16}$$

where **j** is the electrical current density and S_q is the residual-charge volumetric generation rate (C/m^3 s), which arises from the transfer of charge from spray droplets to residual charge species by the mechanisms mentioned earlier. When neglecting the diffusion of the *residual charges*, and from the expression of current density as the sum of gas velocity plus electrophoretic velocity $K \cdot \mathbf{E}$, the equation above becomes

$$\frac{1}{r} \frac{\partial}{\partial r} \left[r C_q \left(K E_r + u_r \right) \right] + \frac{\partial}{\partial z} \left[C_q \left(K E_z + u_z \right) \right] = S_q \tag{17}$$

where C_q is the *residual charge* density (C/m^3) and K is the electrical mobility of *residual charges* (m^2/V s).

The transport equations for vapor and *residual charge* are discretized and solved through an upwind numerical scheme to obtain the respective steady-state background concentrations.

3.3.1.4. Boundary conditions

The boundary conditions when solving for the electrostatic potential ϕ in the region between the capillary tube and the counterplate, were $\phi = \Phi_0$ at the capillary tube and Taylor cone surfaces; $\phi = 0$ V at the plate, $\partial\phi/\partial z = 0$ at $z = -9H$, and $\partial\phi/\partial r = 0$ at $r = 10H$.

The computational domain and boundary conditions for the gasflow are as shown in *Fig. 3.1a*. The surfaces of the capillary tube electrode and the counterplate are assumed to be stationary walls with no-slip conditions. The gas (air) is free to flow in both directions at the open boundaries, with farfield condition on the top boundary at $z = -9H$ and self similarity condition at the side boundary at $r = 10H$ (Deshpande and Vaishnav, 1982). After estimating the diameter of the electrospray jet as d_{jet} from the droplet diameter (Tang & Gomez, 1994; Rosell-Llompart & Fernandez de la Mora, 1994), the surface of the jet is modeled as a cylindrical boundary moving with a uniform velocity V_{jet}, which in turn is estimated from d_{jet} and the total liquid volumetric flow rate Q by mass conservation.

The computational domain and the boundary conditions for the transport of vapor and *residual charges* are shown in *Fig.3.1b.* For the transport of vapor, diffusive flux is absent across the symmetry axis at $r = 0$ as well as across the far field exit boundary at $r = 10H$. We consider fresh gas is constantly entering the domain through the top boundary at $z = 0$, a plane coincident with the exit of electrospray capillary tube, thus $C_V = 0$ on such plane. Additionally on the counterplate, the no-flux boundary condition is imposed.

Residual charges are transported under the combined influence of electric field and gas flow, and hence most of the boundary conditions are implicit by nature of their transport equations. Only required is the specification of zero influx at the top open boundary at $z = 0$.

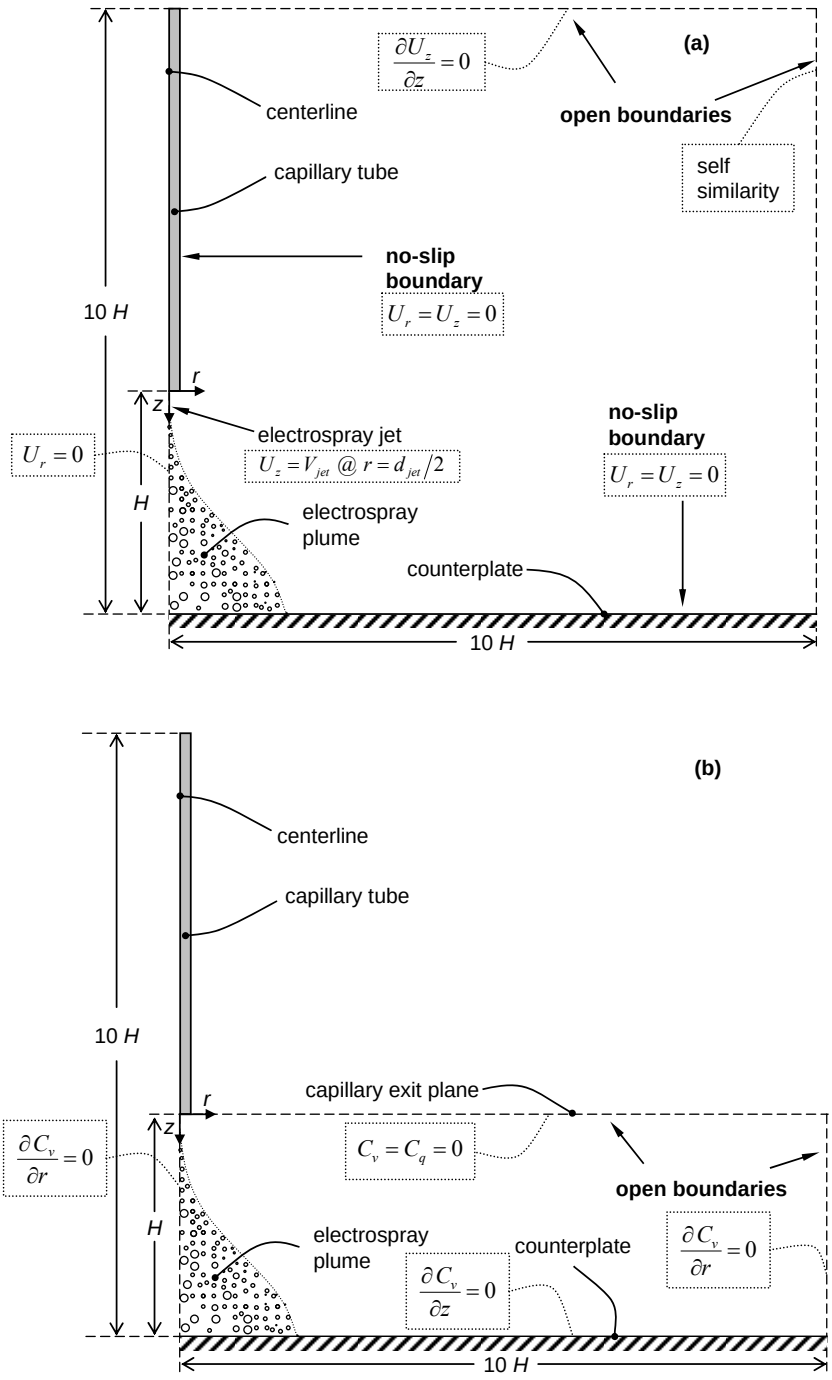

Fig. 3.1. Schematic diagrams of the 2D axisymmetric computational domains for (a) gas flow, and (b) transport of vapor and *residual cha*rge, including the respective boundary conditions

3.3.2. Numerical implementation

The numerical scheme has been implemented in several parts which have been run iteratively through successive stages according to the flow chart shown in *Fig. 3.2*. Initially, quiescent gas with zero background solvent vapor concentration is assumed ($\mathbf{u} = 0$; $C_q = 0$; $C_V = 0$). The droplet dynamics including droplet evaporation and subsequent Coulomb explosions against the input background vapor concentration is simulated for long enough to ensure that a statistically significant portion of the steady state solution is generated.

The droplet dynamics module also computes the generation of *residual charge* as follows. An evaporating droplet shrinks faster as it becomes smaller. The accurate tracking of such shrinking would require time steps that are even smaller than the time step used for tracking the droplet dynamics themselves (Δt). To avoid this additional computational burden, droplets attaining a size below a small *critical diameter* are assumed fully evaporate within a single Δt. In other words, within a single time step, such droplets are assumed to release their remaining solvent mass as vapor into the system, as well as their electrical charge as *residual charge.*

From the droplet dynamics data, an ensemble-averaged drag force density, and a volumetric generation rates of vapor S_V (mols/m^3·s) and of *residual charge* S_q (C/m^3·s) are calculated. Thereafter based on the discretization schemes mentioned in *Section 3.3.1.3*, the steady fields for gasflow, vapor and *residual* charge concentrations are simulated.

Finally, these field values, $\mathbf{u}$, C_V, and C_q, are fed back to the droplet dynamics module (which handles droplet motion, evaporation and Coulomb explosions), thereby completing one stage of iterations for the numerical scheme.

The scheme is considered to have attained global convergence by comparing all the respective fields from two consecutive stages. In the simulations presented in this study, five iterations were needed to ensure global convergence.

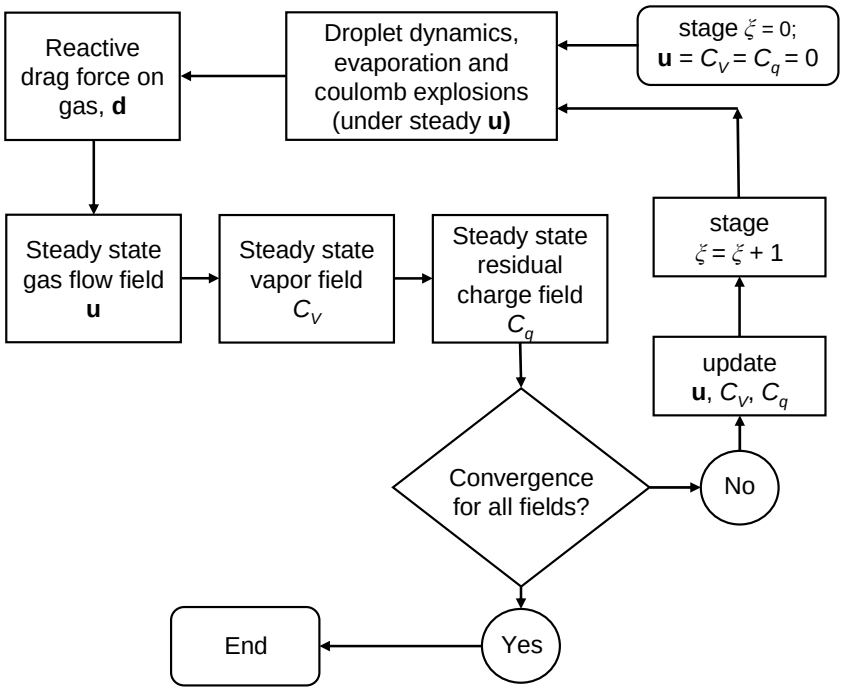

Fig. 3.2. Flow diagram for the fully coupled numerical scheme implemented to simulate volatile electrosprays.

3.4 Results and discussion

3.4.1. Numerical verification

The numerical model for the electrospray droplet dynamics including coulomb explosions was verified by comparing against the results of Wilhelm et. al (2003). Following the simplified approach applied by them to model an n-butanol electrospray system, we overlook the non-equilibrium effects in droplet evaporation, induced airflow, transport of vapor and *residual charge* for this verification. The droplets had a Gaussian size distribution with a root mean square value of 4% and a mean diameter of 19 μm. The volume flow rate was 2.67 ml/h and the electric current 39.3 nA. In this spray system, droplets evaporate against a zero background vapor concentration, subsequently undergoing fission on reaching their Rayleigh charge limits. The ambient gas has a temperature gradient due to the presence of a heated substrate plate held at 673K, at a distance of z = 3 cm from the electrospray nozzle. Mass and charge lost through progenies

are not accounted to modify the background vapor and *residual charge* concentrations. Results from both the simulations are compared in *Fig 3.3*, for which agreement can be observed.

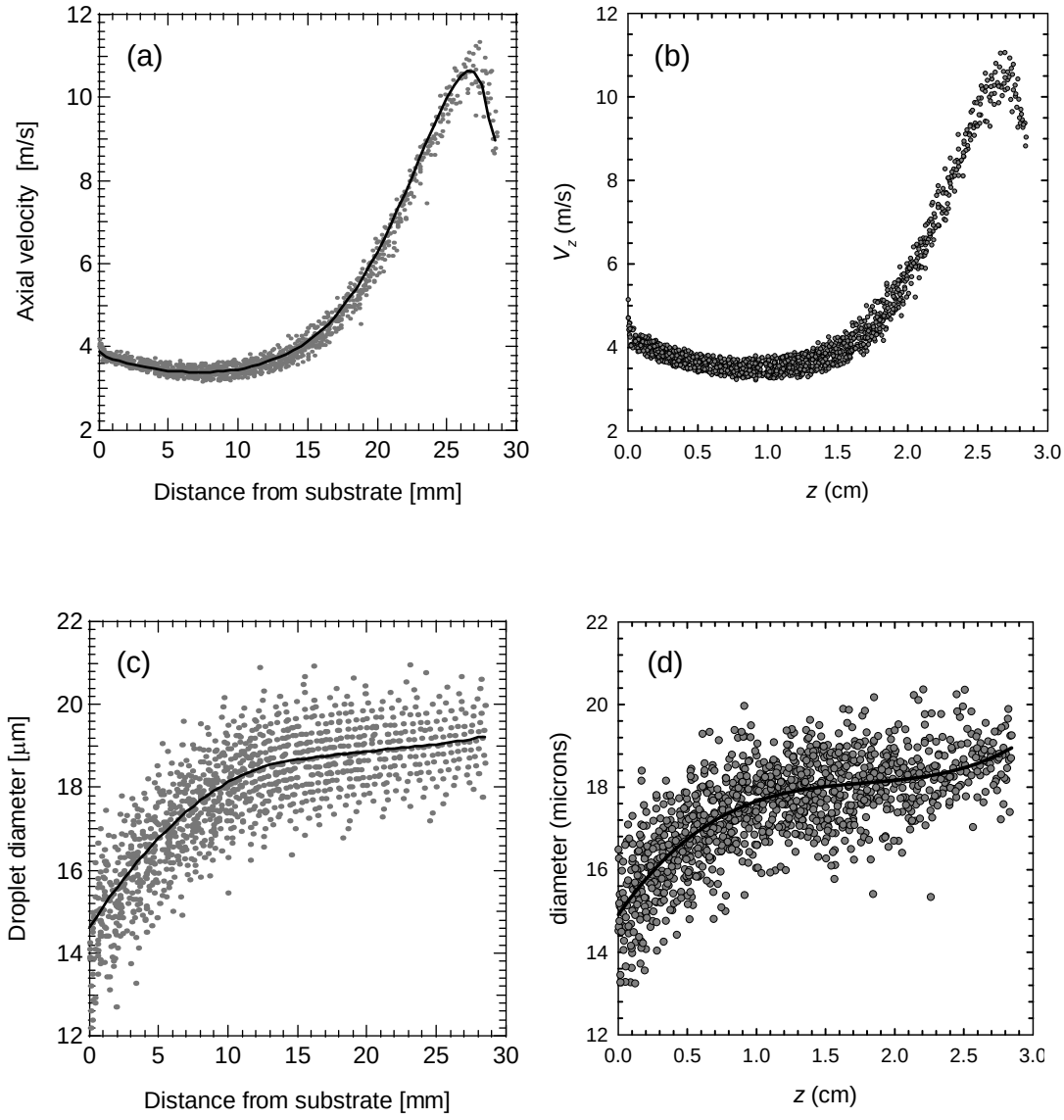

Fig. 3.3. Comparison of results in the simulations for n-butanol spray: **Average droplet velocity** (a) Wilhelm et. al. (2003), (b) present simulations, and **Droplet diameter** (c) Wilhelm et. al. (2003), (d) present simulations. Each data point represents a droplet.

3.4.2. Systems description

The numerical scheme has been applied to simulate three electrospray systems which differ in liquid volatility. All the systems were assumed to have log-normal size distribution with a mean droplet diameter of 8 μm and a coefficient of variation of 10%. The droplets were injected randomly within a radial zone of twice the mean droplet diameter. The values of parameters common to all the three systems are provided in *Table 3.2*. The selection of external voltage Φ_0 was based on the empirical formulae of Smith (1986) and Pantano et. al (1994)

Table 3.2. System configuration

Parameter (units)	Symbol	Value
Capillary-to-plate separation (m)	H	0.03
Capillary-tube OD diameter (μm)	D_c	450
Count mean diameter for droplets (μm)	$\bar{d}$	8.0
Coefficient of variation for droplets	$\sigma_d / \bar{d}$	0.10
Capillary potential (V)	Φ_0	4000

For this comparative study on different electrosprays based on common solvents, we selected acetone, methanol and n-heptane in decreasing order of vapor pressure (*Table 3.3*). In each case, the flow rate, the mean droplet diameter and electrical current were computed based on the empirical formulae of Gañan-Calvo et al (1997). Accordingly, the droplet diameter is a function of flow rate, liquid conductivity, electric current, permittivity, surface tension and liquid density. Conductivity had to be increased significantly in the case of n-heptane, in order to numerically attain the required mean droplet diameter of 8 microns. Such high conductivity for n-heptane electrosprays is well within the feasible experimental limits achieved by means of additives (Tang and Gomez, 1996). It should be noted that the difference in flow rates for the three different systems are small, but could be relevant while analyzing the results of the simulations. The vapor pressure values for the solvents were calculated from the Antoine's equation (Reid et al, 1987).

Table 3.3 Characteristics of the spray systems based on the selected solvents

Sl no.	Solvent	Boiling point T_b (K)	Vap. press. (bars)* @ 300K	Diffusivity in air @300K, Γ x10^4 (m^2/s)	Surface tension, γ (mN/m)	Liquid density, ρ (kg/m^3)	Liquid viscosity, μ (mPas)	Electrical conductivity, K (μS/m)	Flow rate x10^{10} Q (m^3/s)	Current, I (nA)
1	acetone	330	0.333	0.104	23.36	786.0	0.32	20	2.06	42
2	methanol	338	0.187	0.160	22.07	791.8	0.59	44	2.49	55
3	n-heptane	371	0.067	0.070	19.65	684.0	0.40	1.71	1.43	13

*based on Antoine's coefficients for vapor pressure from Reid et al. (1987)

3.4.3. Systems simulation

For all the three spray systems mentioned in *Table 3.3*, the electric field was computed using a very fine non-homogeneous grid of 337×505 cells extending *10H×10H*, of which a domain under *z=0* is used to compute the transport of *residual charge* (*Fig.3.1*). The induced gasflow computations were performed using a non-uniform grid of 193×252 cells extending *10H×10H*. This grid had the smallest radial cell size of $d_{jet}/2$ at the symmetry axis, and the smallest axial cell size of 45 μm both at the counterplate and at the capillary tube tip.

Based on the discussion in *Section 3.3.1.2*, we have assumed that droplets undergo Coulomb explosions on reaching their charge limit releasing 2% of their mass ($\Delta m/m$ = 0.02) in 4 progenies, each in turn carrying a charge 70% of its own Rayleigh limit (α = 0.7). Considering the first Coulomb explosion can happen when the parent droplet is about 6 microns in diameter, each progeny will have a diameter of 1.025 μm. In the simulations, we consider 1.025 μm as the *critical diameter*, at which in our scheme a droplet turns into a *residual charge* and solvent vapor (*Section 3.3.2*).

In our simulations we have chosen to treat *residual charges* as *monomobile* species, for the sake of simplicity. Depending upon the solute and (or) purity of solvent in an electrospray application (Karpas, 1989; Rosell, 1994; Steiner et al, 2001; Kirby, 2009; Fernandez-Maestre, 2010), the species carrying the residual charge can have a wide range of electrical mobility. For a spherical *residue* at charge limit ratio α, one can compute its electrical mobility (K) by the relation:

$$K = \frac{\alpha q_R C_c}{3\pi\mu_g d} \tag{10}$$

Fig. 3.4 shows the variation in electrical mobility depending on the size of a spherical *charged residue* for α= *0.7* Hence for the residues of the *critical diameter*, the electrical mobility cannot be below 0.14 cm^2/V s. Considering this and with reference to the literature mentioned above, we employ a uniform electrical mobility K of 0.5 cm^2/V-s in all the three systems simulated.

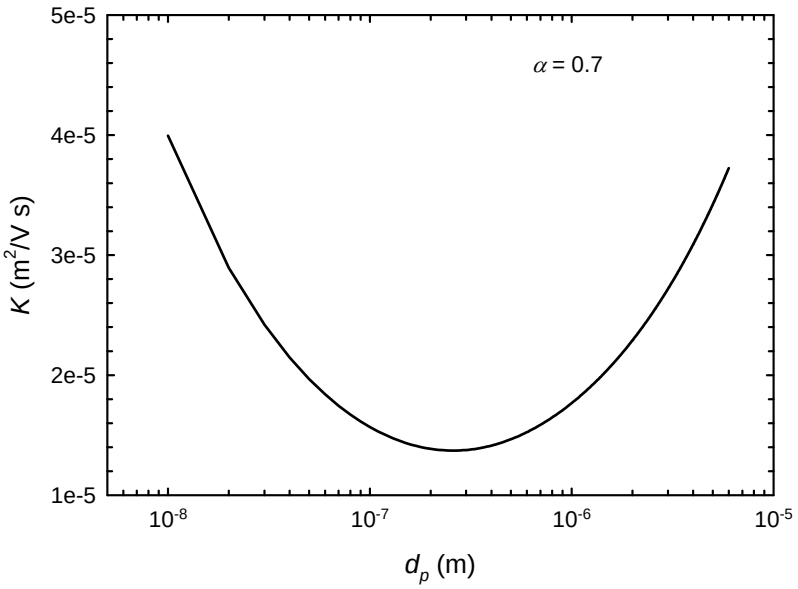

Fig. 3.4. Electrical mobility vs. sphere diameter at a *residue* charge limit of 70%

The time step for droplet dynamics computation is 1×10^{-6} s, whereas the calculations for droplet evaporation is carried out once in every 20 Lagrangian time steps (i.e. 2×10^{-5} s). Preliminary simulations on the single droplet evaporation for all the solvents at an average axial gas velocity of 3 m/s (identified through the gasflow computations), revealed that less than 2×10^{-5} s is required for the complete evaporation of a droplet of size below the *critical diameter*, justifying the choice of this evaporation time step. All droplets dynamics data feeding into the other parts of the simulation were computed by ensemble averaging the droplet dynamics results within the period 0.1s to 0.2s of spray-simulation time, which corresponds to 500 snapshots of the electrospray system.
The simulation results of the three different systems are reported separately hereafter.

3.4.3.1 Acetone electrospray

The streamlines for steady-state induced airflow on attaining convergence after five stages (global iterations, see *Fig. 3.2*) are shown in *Fig. 3.5a*, along with one snapshot of the acetone electrospray system. The steady state field for vapor concentration,

transported combinedly through convection and diffusion, under the influence of airflow is depicted in *Fig. 3.5b*.

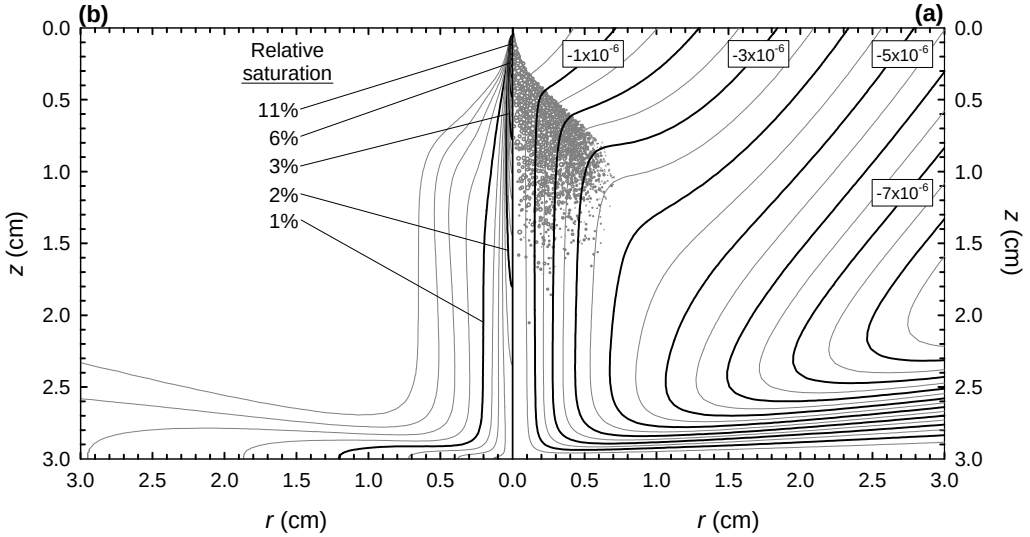

Fig. 3.5. (a) Snapshot of evaporating acetone electrospray with streamlines of induced airflow, and (b) steady state vapor iso-concentration contours as % of saturation concentration (for air at 300K).

A maximum vapor concentration is observed at the droplets emission point owing to the highest droplet concentration involved. The concentration decreases steeply radially and axially, practically representing a situation of almost zero background vapor concentration for the major part of the spray. Comparative simulations shows that while this spray have only 2500 droplets, a non-evaporating spray of the same solvent had around 15000 droplets, both evaluated at steady state configurations. Practically all of the spray is completely evaporated within an axial distance of 2 cm from the needle.

The axial induced airflow velocity at the spray axis drops from 14.7 m/s at the electrospray jet moving with the same velocity, to 3 m/s within an axial distance of 3 mm from the needle and remains around 2 m/s thereafter before dropping to zero close to the substrate plate. Considering an average axial airflow velocity of 2 m/s, the Peclet number $Pe = \Delta z U_z / \Gamma >> 1$ for the present system. Here Δz is the needle to plate distance, U_z a representative axial velocity of air within the spray volume and Γ the diffusivity of acetone vapor in air. Hence most of the vapor transport is dominated by convection

instead of diffusion, and basically follow the streamlines. This explains the narrow radial spread of vapor within the domain even though the droplets experience rapid evaporation (*Fig. 3.5a*).

Fig. 3.6a shows the overall rate at which *residual charge* is generated per unit volume (S_q) within the spray due to droplet evaporation and subsequent Coulomb explosions. Three stages of Coulomb explosions are identifiable from this contour plot as regions of high S_q. The transport of *residual charges* is collectively influenced by the electric field and the airflow. The steady state concentration field for the *residual charge* is shown in *Fig. 3.6b*. Since *residual charges* are generated through Coulomb explosions occurring simultaneously at multiple locations within the spray, and due to the decrease in radial velocities of such charges in accordance with the local radial electric field ($U_{r,q}=KE_r + U_r$), we observe their concentration to be higher towards the periphery of the electrospray.

The redistribution of space charge and hence the electric field due to the presence of the *residual charge* within the electrospray has been included in the droplet dynamics computations. However since the mobility of the *residual charge* is very high in comparison with the charged droplets, their residence time was shorter and hence was not found to any significant influence in the overall droplet dynamics.

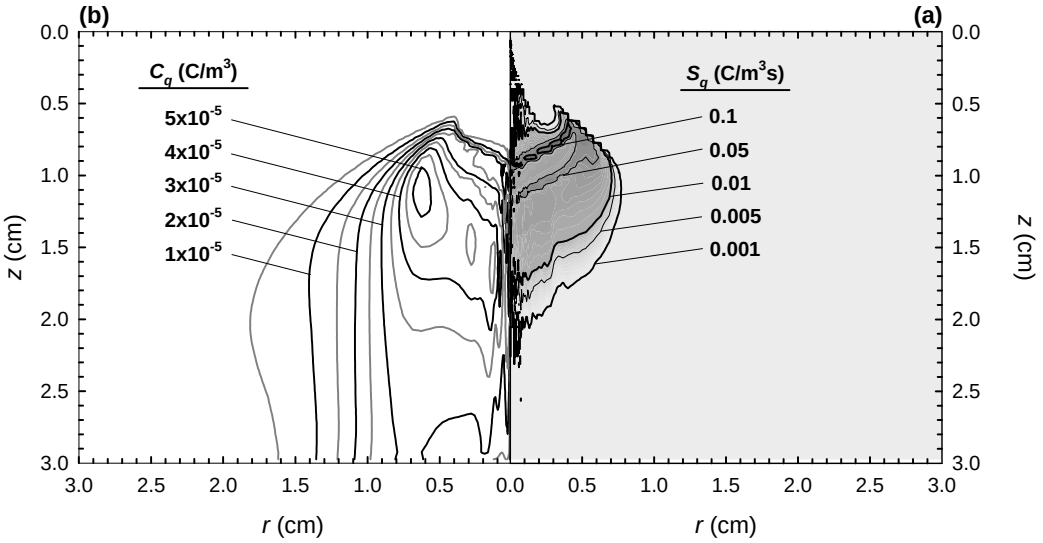

Fig. 3.6. Contour plots of (a) *residual charge* volumetric generation rate (S_q), depicting regions of Coulomb explosions, and (b) *residual charge* concentration, for acetone electrospray at steady state.

3.4.3.2 Methanol electrospray

The methanol electrospray had a higher jet velocity of 17.6 m/s in comparison with that of acetone spray. Axial velocity of induced airflow dropped from jet velocity at needle and averaged around 2 m/s thereafter. The electrospray reduced from around 16000 droplets to 8000, once evaporation due to induced gasflow was included in the computations (*Fig. 3.7a*). A maximum of about 14% to methanol vapor saturation concentration in air (at 300K) was identified close to the spray emission region (*Fig. 3.7b*). Liquid flux below 1% of the emitted solvent volume reached the substrate plate, signifying practically complete evaporation of the spray. Though methanol has a higher diffusivity in air (0.16 cm^2/s at 300K) than acetone, a high Peclet number suggests that vapor transport by convection is dominant in this system too, which follows the streamlines of airflow (*Fig. 3.7b*). However, on comparison it is evident that the methanol spray system has greater radial spread in vapor concentration than the acetone spray, which we attribute to the following reasons. The larger flow rate and lower vapor pressure in comparison with acetone as the solvent, contributes to lesser evaporation and thereby more droplets within the spray. Owing to higher electrical conductivity and hence higher electric current carried (*Table 3.3*), the larger number of droplets gives rise to higher spray space charge. Higher space charge leads to greater mutual repulsion among droplets and hence the greater spread in evaporating plume and resulting vapor field.

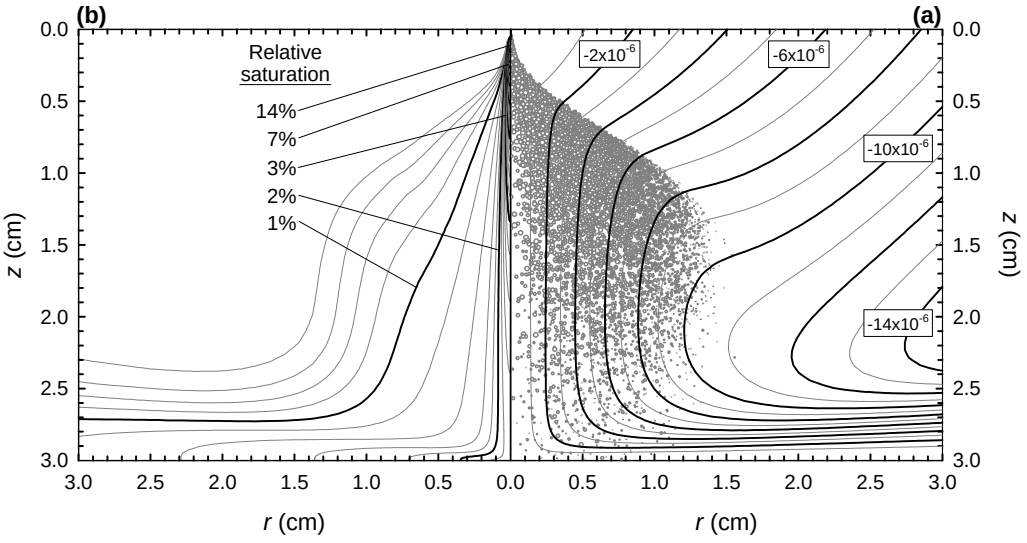

Fig. 3.7. (a) Snapshot of evaporating methanol electrospray with streamlines of induced airflow, and (b) steady state vapor iso-concentration contours as % of saturation concentration (for air at 300K).

A larger plume for the present system means that some of the Coulomb explosions occur close to the counter-plate (see *Fig 3.8a*). Upto three such regions are observed in the *Fig 3.8a*, signified by high S_q. For this spray system, *residual charges* were significant and in the same order as the charge carried by the droplets themselves. However owing to the larger volume occupied by them in comparison with the droplets, contribution to the aerodynamic drag force density due to their motion was very small. Hence they didn't significantly alter the induced gasflow field computed only from the droplet motion.

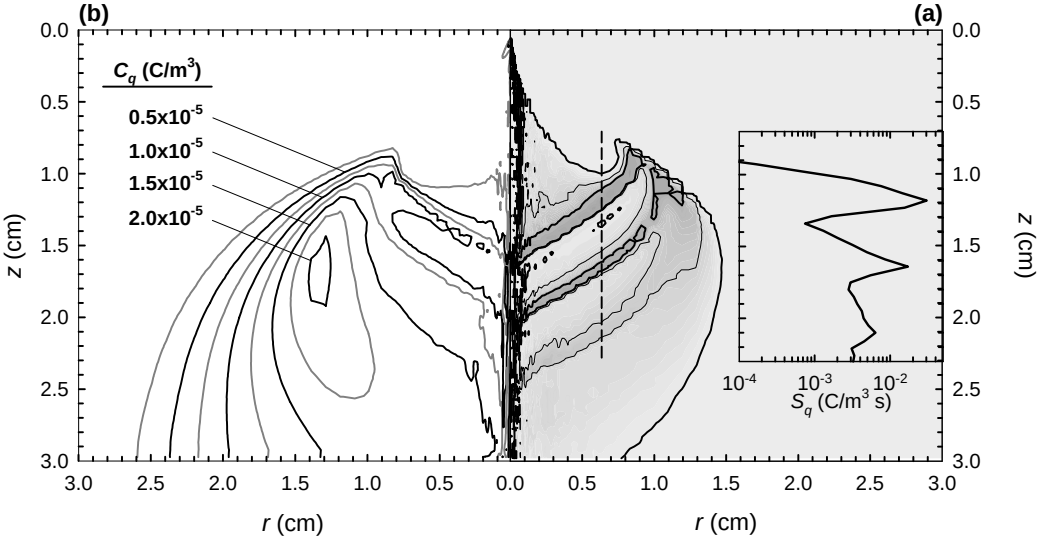

Fig. 3.8. Contour plots of (a) *residual charge* volumetric generation rate (S_q), depicting regions of Coulomb explosions, and (b) *residual charge* concentration, for methanol electrospray at steady state.

3.4.3.3 n-heptane electrospray

N-heptane has moderate vapor pressure, and was the least volatile among the three solvents selected for comparison. For the designed electrospray system of mean droplet size 8 μm, the current carried was substantially lower. Also the flow rate maintained for

the heptane spray in cone jet mode is only about half of the other two systems (see *Table 3.3*). Since charge carried by an electrospray droplet is given by $q = (I/Q) \times (\pi d^3/6)$, the heptane droplets carried lower charges and hence moved much slower in comparison with those in the other systems. The electrospray had a jet velocity of only 10.14 m/s which coincides with the initial axial velocity of droplets. After an initial slight increase, this drops to an average axial velocity of about 2.5 m/s, whereas the centerline airflow velocity drops from the electrospray jet velocity to an average of under 1.5 m/s.

The spray evaporated completely before reaching the substrate plate and had around 2400 droplets (*Fig.3.9a*) instead of the 21000 droplets for the same configuration, simulated without considering evaporation. The vapor concentration is low as in the other systems and has a maximum of around 15% close to the needle. Peclet number analysis indicates convective transport of vapor is dominant as in the other two systems. Also a smaller count of droplets meant lesser spray charge, hence a narrower plume and vapor field confined along the streamlines (*Fig. 3.9b*). However considering the low volatility of n-heptane, the results indicating complete evaporation of droplets are intriguing and require further discussion as follows. To check the possibility of complete evaporation of droplets as observed in our study, we use the basic D^2 law on the experimental data of Burris (1954) who investigated the evaporation characteristics of n-heptane droplets in air stream at various flow conditions. Accordingly, time to evaporate an isolated 8 micron n-heptane drop completely for similar ambient conditions and airflow velocity is around $5x10^{-4}$ s, while even the fastest droplets in the present system have a residence time of $1.2x10^{-2}$ s (~ 24 times the former) owing to the lowest charge content of spray. Hence the results of the simulation are justified.

Broad region of Coulomb explosions in close proximity are observed for the slow moving spray system (*Fig 3.10a*). The final steady state concentration of *residual charge* (*Fig 3.10b*) is of lower intensity compared to the other two systems owing to the lower charge carried by the droplets in comparison, and the uniform electrical mobility assumed for the *residual charge* in all the simulations. In other words, this system comparatively creates lesser *residual charges* on full evaporation of its droplets, which in turn tend to move towards the counter-plate as fast as in the other two systems due to their assumed uniform mobility.

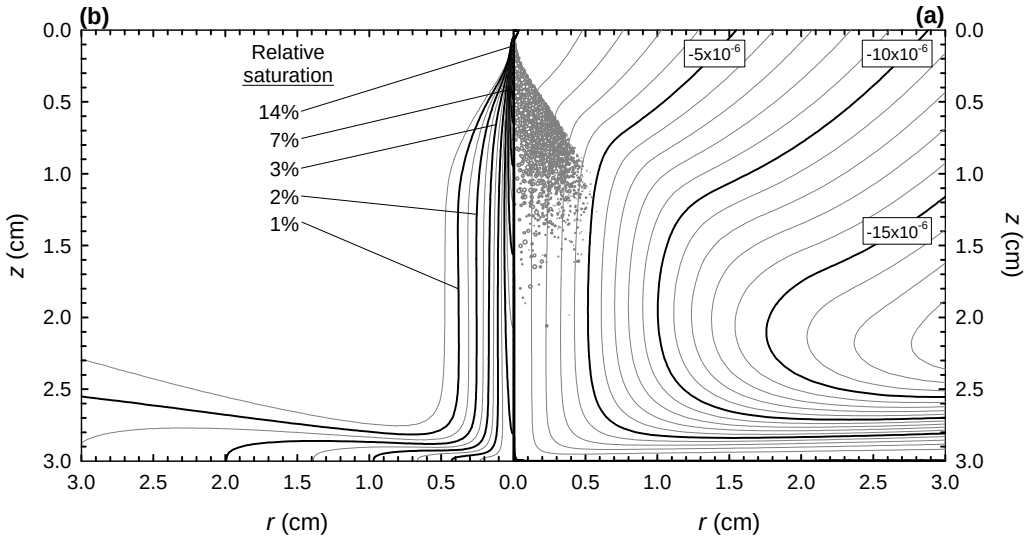

Fig. 3.9. (a) Snapshot of evaporating n-heptane electrospray with streamlines of induced airflow, and (b) steady state vapor iso-concentration contours as % saturation concentration (for air at 300K).

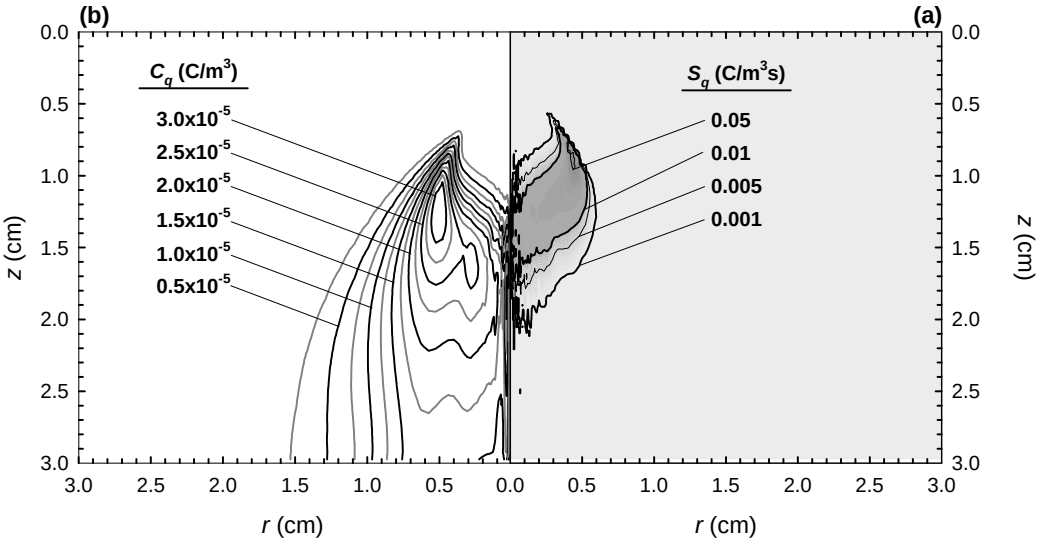

Fig. 3.10. Contour plots of (a) *residual charge* volumetric generation rate (S_q), depicting regions of Coulomb explosions, and (b) *residual charge* concentration, for n-heptane electrospray at steady state.

3.5 Conclusions

A numerical scheme has been developed for volatile electrospray systems, which for the first time fully couples electrospray droplet dynamics with the effects of induced airflow, Coulomb explosions, and the transport of solvent vapor as well as re*sidual charge*. After validating the results with other non-coupled simulations of an evaporating electrospray in stagnant conditions, the scheme is elaborated by introducing non-equilibrium effects in droplet evaporation, along with the encompassing dynamic effects of induced gasflow. The model was applied to compare the evaporation effects on the characteristics of three electrospray systems of varying volatility, but with same mean droplet size and similar input conditions. Results show that induced gasflow is a very important factor in the droplet evaporation when the droplet sizes are in the range common to electrospray applications. The results also suggest that the vapor transport in such systems is mainly due to forced convection instead of diffusion. Vapor transport by pure diffusion has been a simplified approach commonly followed in the numerical simulations of evaporating electrosprays due to the assumption of stagnant ambient conditions. By being able to predict the source and extent of vaporization, as well as the *residual charges*, we assume that this numerical scheme will have greater applicability if extended to the field of electrospray-ionization mass spectrometry, with appropriate changes in the gasflow conditions (for eg. co-axial, heated, vapor saturated etc.).

3.6 References

Abramzon, B., & Sirignano, W. A. (1989). Droplet vaporization model for spray combustion calculations. *Int. J. Heat and Mass Tr.*, *32*, 1605–1618.

Arumugham-Achari, A.K, Grifoll, J., & Rosell-Llompart, J. (2013). Two-way coupled numerical simulation of electrospray with induced gas flow. *J. Aer. Sci., 65,* 121–133.

Bock, N., Dargaville, T.R., & Woodruff, M.A. (2012). Electrospraying of polymers with therapeutic molecules: state of the art. *Progress in Polymer Science*, 37, 1510–1551

Bodnár, E., & Rosell-Llompart, J. (2013). Growth dynamics of granular films produced by electrospray. *Journal of Colloid and Interface Science*, 407, 536–545.

Davis, E. J., & Bridges, M. A. (1994). The Rayleigh limit of charge revisited: Light scattering from exploding droplets. *J. Aer. Sci.*, *25*, 1179-1199

Fenn, J.B., Mann, M., Meng, C.K., Wong, S.F., & Whitehouse, C.M. (1989). Electrospray ionization for mass spectrometry of large biomolecules. *Science*, 246 (4926), 64–71

Fenn, J.B., Rosell, J., Nohmi, T., Shen. S., & Banks Jr., J.F. (1996). Electrospray Ion Formation: Desorption versus Desertion, *American Chemical Society Symposium Series*, 619, 60-80

Fernández de la Mora, J. (1996). On the Outcome of the Coulombic Fission of a Charged Isolated Drop. *Journal of Colloid and Interface Science*, *178*(1), 209–218.

Gañán-Calvo, A. M., Dávila, J., & Barrero, A. (1997). Current and droplet size in the electrospraying of liquids. Scaling laws. *Journal of Aerosol Science*, *28*(2), 249–275.

Gañan-Calvo, A. M., Lasheras, J. C., Dávila, J., & Barrero, A. (1994). The electrostatic spray emitted from an electrified conical meniscus. *J. Aer. Sci.*, *25*, 1121–1142

Gosman, A. D., Pun, W. M., Runchal, A. K., Spalding, D. B., & Wolfshtein, M. (1969). *Heat and mass transfer in recirculating flows*. Academic Press Inc.: London.

Grifoll, J. & Rosell-Llompart, J. (2012). Efficient Lagrangian simulation of electrospray droplets dynamics. *J. Aeros. Sci., 47*, 78-93.

Grifoll, J. & Rosell-Llompart, J. (2014). Continuous droplets' charge model for the Lagrangian simulation of 2 electrostatic sprays, *submitted to J. Electrostatics*

Grimm, R.L, & Beauchamp, J. L. (2002) Evaporation and Discharge Dynamics of Highly Charged Droplets of Heptane, Octane, and p-Xylene Generated by Electrospray Ionization. *Anal. Chem*., *74*, 6291-6297.

Gu, W., Heil, P. E., Choi, H., & Kim, K. (2007). Comprehensive model for fine Coulomb fission of liquid droplets charged to Rayleigh limit. *Applied Physics Letters*, *91*(6), 064104.

Hinds, W. C. (1999). *Aerosol technology: properties, behavior, and measurement of airborne particles*, 2nd ed.; John Wiley and Sons: NewYork.

Hogan, C. J., Biswas, P., & Chen, D. (2009). Charged droplet dynamics in the submicrometer size range. *The Journal of Physical Chemistry. B*, *113*(4), 970–6.

Hunter, H. C., & Ray, A. K. (2009). On progeny droplets emitted during Coulombic fission of charged microdrops. *Physical Chemistry Chemical Physics*, *11*(29), 6156–65.

Jakubczyk, D., Kolwas, M., Derkachov, G. , Kolwas, K., & Zientara, M. (2012) Evaporation of Micro-Droplets: the "Radius-Square-Law" Revisited. *Acta Physica Polonica A*, *122*, 709-716

Jaworek, A., & Sobczyk, A.T. (2008).Electrospraying route to nanotechnology: an overview. *J. Electrostat*, 66, 197–219.

Kebarle, P. & Tang, L. (1993) From ions in solution to ions in the gas phase: The mechanism of electrospray mass spectrometry. *J. Analytical Chem*., *64*(22), 972-986

Li, K.-Y., Tu, H., & Ray, A. K. (2005). Charge Limits on Droplets during Evaporation. *Langmuir*, *21*(9), 3786–3794.

Miller, R.S., Harstad, K., & Bellan, J. (1998). Evaluation of equilibrium and non-equilibrium evaporation models for many-droplet gas-liquid flow simulations. *Int. J. Mult. Flow*, *24,* 1025-1055.

Pantano, C., Gañán-Calvo, A. M., & Barrero, A. (1994). Zeroth-order, electrohydrostatic solution for electrospraying in cone-jet mode. *Journal of Aerosol Science*, *25*(6), 1065-1077.

Ried, R.C., Prausnitz, J. M., & Poling, B. E. (1987). *The properties of gases and liquids: Fourth ed*., McGraw-Hill Inc

Rietveld, I.B., Kobayashi, K., Yamada, H., & Matsushige, K.(2006). Electrospray deposition, model, and experiment: toward general control of film morphology. *Journal of Physical Chemistry B*, 110, 23351–23364.

Rosell-Llompart, J. & Fernandez de la Mora., J. (1994). Generation of monodisperse droplets 0.3 to 4 μm in diameter from electrified cone-jets of highly conducting and viscous liquids. *J. Aeros. Sci., 25*(6), 1093-1119

Roth, D. G., & Kelly, A. J. (1983) Analysis of the disruption of evaporating charged droplets. *IEEE Transactions on Industry Applications*, *IA-19*, 771–775.

Sazhin, S.S (2005) Modelling of heating, evaporation and ignition of fuel droplets: combined analytical, asymptotic and numerical analysis. *Journal of Physics: Conference Series*, *22,* 174–193

Sazhin, S.S (2006) Advanced models of fuel droplet heating and evaporation *Progress in Energy and Combustion Science*, *32*, 162–214

Sen, A.K., Darabi, J., & Knapp, D. R. (2011) Aerosol Formation in Electrospray Ionization Using a Microfluidic Emitter. *IEEE Sensors Journal, 11*(10), 2335-2341

Smith, J. N., Flagan, R. C., & Beauchamp, J. L. (2002) Droplet Evaporation and Discharge Dynamics in Electrospray Ionization. *J. Phys. Chem. A*, *106***,** 9957–9967

Smith, D. P. H. (1986). The Electrohydrodynamic Atomization of Liquids. *IEEE Transactions on Industry Applications*, *IA-22*(3).

Taflin, D. C., Ward, T. L., & Davis, E. J. (1989). Electrified droplet fission and the Rayleigh limit. *Langmuir*, *5*(2), 376–384.

Tang, K., & Gomez, A. (1994). On the structure of an electrostatic spray of monodisperse droplets. *Physics of Fluids*, *6*(7), 2317.

Tang, K., & Gomez, A. (1996). Monodisperse Electrosprays of Low Electric Conductivity Liquids in the Cone-Jet Mode. *Journal of Colloid and Interface Science*, *184*(2), 500-511.

Tang, K., & Smith, R. D. (1998). Theoretical prediction of charged droplet evaporation and fission in electrospray ionization. *Int. J. Mass Spec.*, *185/186/187*, 97-105.

Wilhelm, O., Mädler, L., & Pratsinis, S. E. (2003). Electrospray evaporation and deposition. *Journal of Aerosol Science*, *34*(7), 815–836.

Chapter 4

Chapter 4

Conclusion

A numerical scheme which includes the gasflow induced by droplet motion in the numerical simulation of electrosprays has been developed. Applying this computational scheme initially on a non-volatile electrospray system, steady state solutions were sought iteratively by fully coupling a 3D Lagrangian model for the droplet dynamics with a steady state 2D axisymmetric Eulerian model for the induced gas flow.

To resolve the reactive drag force on the gas by the droplets we employ Gaussian filters with variable kernel widths that depend on the droplet number density. At the denser spray regions close to the droplet emission point, we argue that the kernel size should neither be much wider nor much smaller than the average droplet diameter. Further downstream, where the droplet number density decreases, a wider kernel width has been used in order to suppress the fluctuations in the reactive force density.

In order to quantify the effect of induced gasflow on the characteristics of the droplet plume (viz., droplet number density, droplet velocity, droplet size distribution), as well as on droplet dynamics and mass flux, we applied this scheme to an experimentally characterized spray by Tang & Gomez (1994), which comprised of non-evaporating primary and satellite droplets in air.

Results show that including air motion in the simulations modifies the droplet trajectories significantly. Radial profiles of number density, and of local average droplet diameter, and centerline droplet velocities show better agreement with the experimental data when airflow is taken into account than when it is not (assuming still air). Significant air entrainment towards the spray axis is observed near the droplet generation region, which develops into a jet like structure that impinges onto the counterplate. The droplets mass flux radial distribution is particularly sensitive to the air entrainment, which results in a steep increase near the spray axis. It is shown that the induced airflow contributes to faster moving droplets, shrinkage of plume, and a prominent flux about the spray axis (centerline), as compared with the simulations assuming still air. We have also observed that the radial segregation by size of the satellite droplets is sensitive to the functional relationship between their charge-to-mass ratio and diameter.

Since electrospray applications usually involve volatile spray systems and gasflow being an important aspect in droplet evaporation, we further developed a comprehensive numerical scheme which fully couples the Lagrangian electrospray droplet dynamics with the effects of induced gasflow, Coulomb explosions, and the transport of solvent vapor as well as charge left over by vanishing droplets in volatile electrospray systems. Separate codes for the diverse phenomena were developed to achieve the same.

To couple the different physics, the Lagrangian code and the three Eulerian ones (for the dynamics of gasflow, vapor and charge left by fully evaporating droplets) were run sequentially, taking the inputs needed for each code from the results of the preceding runs. The Eulerian codes were formulated under steady state, while for the Lagrangian model we take an ensemble average of a steady-state portion of the simulation as representative. After several sequences of simulations, each variable field converged and the overall result was taken as illustrative of the behavior of the electrospray under steady state.

This methodology has been applied to compare the evaporation effects in three electrospray systems with solvents of different volatility: acetone, methanol and n-heptane. The droplets were injected into the three systems with unimodal and log-normal distributed diameters with a mean value of 8 μm, and a coefficient of variation of 10%. Regions of intense Coulomb explosion events in form of diagonal bands (in the 2D domain) within the spray are well captured. We observe that the vapor transport in these mechanisms are predominantly by forced convection rather than diffusion. Highest vapor concentration is observed near the injection zone for all the three systems, which rapidly decays thereafter, both radially as well as axially. In all three cases, few or no droplets arrive at the counterplate located 3 cm down the capillary nozzle, highlighting the relevance of accounting for evaporation when simulating these systems.

By being able to predict the source and extent of vaporization, as well as the concentration of charge released by vanishing droplets, we assume that this numerical scheme will have greater applicability if extended to the field of electrospray-ionization mass spectrometry, with appropriate changes in the gasflow conditions (for eg. co-axial, heated, vapor saturated etc.).